II.2. Optimization of nSL process on CMOS: alignment and blurring corrections

Our global fabrication strategy of nanodevices on CMOS is based on using existing CMOS layers as structural layer (600 nm thick polysilicon) and sacrificial layer (1 µm thick field oxide) of the resonators. This strategy simplifies the processing and facilitates the further electrical contact between the nanomechanical devices and the circuits [1, 2]. After concluding CMOS circuits fabrication, integration areas are patterned by evaporation of 80 nm of aluminum using nSL. At this stage, several challenges concerning nSL and its related fabrication process steps were identified at the beginning of the project.

Concerning nSL itself, issues like the alignment between CMOS wafer and nanostencil wafer, clamping uniformity, blurring effect (pattern widening), membrane stability, clogging and cleaning (reusability) have been identified.

In the present work, we have focused on addressing two processing challenges: (i) alignment between CMOS wafer and nanostencil wafer and (ii) elimination of pattern blurring. Indeed, as previously mentioned, a major limitation in nSL is gap-induced pattern blurring naturally occurring if a planar stencil is used in combination with a substrate containing topography (e.g. CMOS). The characterization of this phenomenon has been undertaken and a corrective technique has been implemented. These two issues are detailed in next sections.

Membrane stability was solved by fabricating corrugated membranes (see section I.1.b). Clogging and cleaning issues are still being characterized at EPFL.

Regarding related process steps (prior or posterior to nSL), various dry etchings of either dielectric or polysilicon layers have been optimized in the framework of this thesis. For this purpose, special test wafers with similar topography to CMOS substrates were designed and fabricated. They will be described in section II.2.c.

II.2.a. Alignment

In order to match the stencil nano/micropatterns with the integration areas contained in the CMOS substrate, full-wafer nanostencil (nS) and CMOS wafer (both 100 mm diameter) must be aligned one to each other before evaporation of metal through nanostencil apertures. An alignment procedure is established that leads at the end to the rigid clamping of both aligned elements into one portable piece that can be placed into the evaporation chamber.

This operation is performed within a bond aligner SÜSS MICROTEC MA/BA6, equipped with two microscopes, for which a special chuck was designed by SÜSS MICROTEC. This chuck responds to several requirements: it can be inserted in the mask aligner and after optical alignment it mechanically clamps rigidly stencil and substrate at three different sites; therefore they can be transported with safety, i.e. without relative motion, to the evaporation chamber and be fixed inside. Moreover, this chuck allows moving one element with respect to the other, which is fixed, while a thin controllable gap (down to 15 µm) is maintained between both objects, in order to ensure good optical visualization (optical focus can be achieved almost simultaneously).

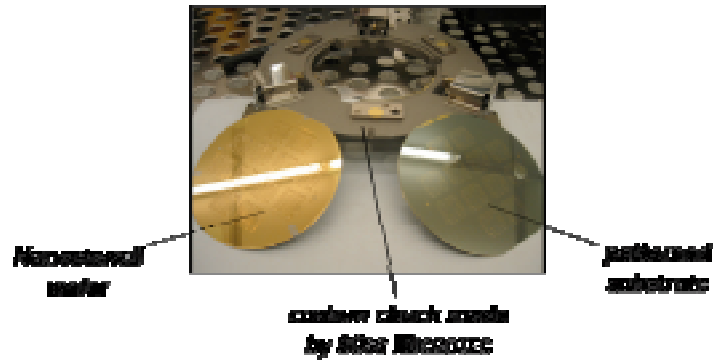

Figure 9. Custom chuck developed by SÜSS MICROTEC for the purpose of optically aligning a 100 mm nS wafer to a 100 mm substrate and then clamping at 3 points for transportation to the evaporation chamber

Special patterns, called alignment marks (*AM*), were foreseen in both layouts of nS and CMOS substrates in order to allow optical alignment. They have been designed to reach a 1 µm accurate alignment at 100 mm wafer scale. Alignment marks contained in CMOS substrates and used to align one reticule to another during CMOS process were not utilized (moreover, dicing lines area is too reduced). For the purpose of aligning nanostencils to CMOS wafers, specific alignment marks were designed and included inside the chip layout (see Figure 10 and Figure 5). There are two sets of alignment marks per chip: one made of *poly0* (grey circle in Figure 10), another made of *metal* (black circle in Figure 10 with zoom). Both have an identical design, depicted in the zoom of next figure. Taking into account that the vision area is restricted by the limited motion of the two microscopes, eight sets per whole wafer are potentially visible in each objective.

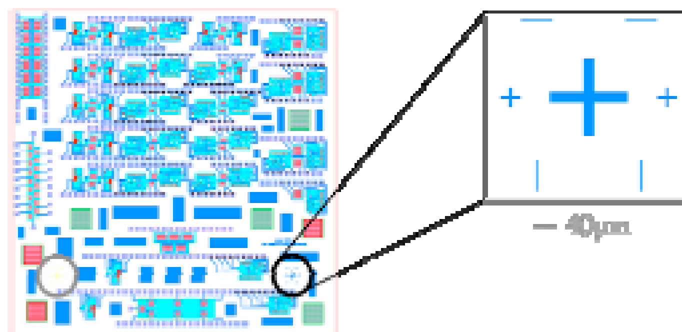

Figure 10. Alignment marks design and positions within the CMOS chip layout.
Grey circle: *AM* made of poly0; Black circle and related zoom: metal *AM*.

The alignment marks included in the nanostencil layout have a complementary design for an enhanced alignment. Figure 11 contains two optical images taken during the alignment procedure within the mask aligner when both elements are being aligned and are still separated by a thin controllable gap that is small enough to ensure simultaneous visualization of membrane and substrates. The alignment marks of CMOS substrate can be observed through nanostencil apertures.

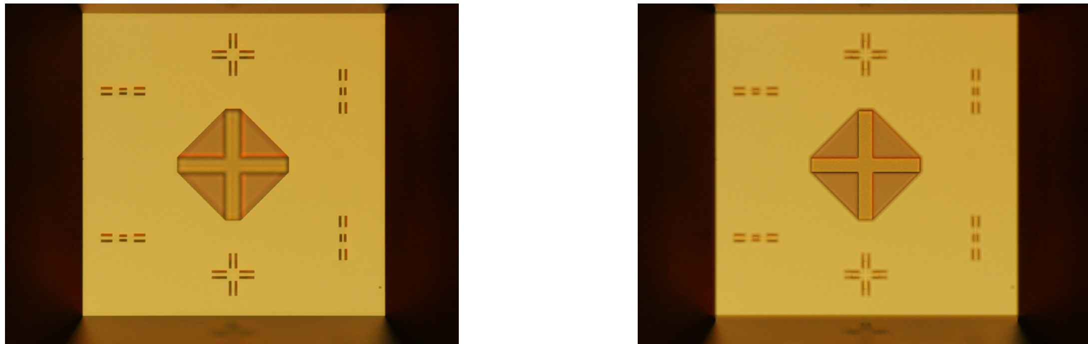

Figure 11. Optical image of a SiN membrane (in yellow) accessed by KOH wet etching through the Si frame (in black). Underneath *AM* of CMOS substrate are visible through the membrane apertures. Left image: focus on the membrane. Right image: focus on the CMOS substrate.

The experimental results of this procedure in terms of implementation and accuracy are detailed in section II.3.b.

Once stencil and substrate are aligned, the chuck clamps one element to the other without lateral displacement and with a sufficient pressure that impedes any misalignment during transportation of the piece and its fixing into the evaporation chamber.

II.2.b. Blurring of Al patterns deposited by nSL

In our process, the patterns deposited by nSL serve as etch mask for pattern transfer to the polysilicon structural layer by reactive ion etching (RIE). In this context, aluminum (Al) has been chosen as pattern material for two reasons. First, its RIE selectivity with respect to silicon and silicon oxide is very high even for very thin Al layers; second, due to its specific properties in terms of blurring compared to other materials like Cu.

Hereafter, the characteristics of the blurring behavior of Al deposits is detailed.

CHARACTERISTICS OF BLURRING EFFECT [31]

When a nanostencil and a wafer are put in contact, the gap between nanostencil membranes and substrate areas to be patterned varies from 0 to several microns depending on substrate curvature and topography. Disregarding surface migration considerations, a non-zero gap generates a blurring of the resulting pattern by a geometrical dispersive effect schemed on Figure 12:

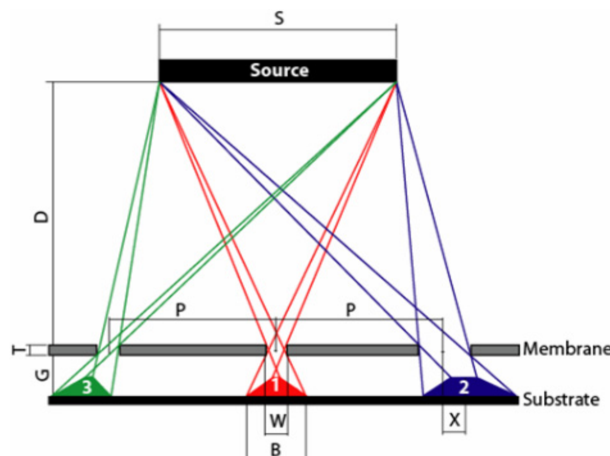

Figure 12 [5]. Metal flux scheme during evaporation of a metal patterned by nanostencil lithography

- D = 100 cm is the source-stencil distance
- S = 2 cm is the source diameter
- T = 200 nm is the stencil thickness
- G is the gap stencil-substrate. G is nominally around 3.1 µm high: the maximum height between the bottom of an 'integration area' (i.e. deposition area, *poly0*/gate oxide stack) and the top of the substrate on which the nS membrane leans on, is equivalent to an interlevel oxide/metal/passivation stack (1.3 + 1 + 0.8 µm high in total). This can be measured with a profilometer. After clamping the nanostencil wafer to the CMOS substrate, G may be locally larger because of the eventual inclusion of particles and because of wafer tolerances (e.g. wafer curvature).
- W is the stencil aperture size
- B is the resulting pattern size on the substrate
- P is the distance from central apertures to lateral apertures (in our case 5 cm is a maximum since we use 100 mm wafers)
- X is the displacement of the deposited structure

The blurring extension on each side can be quantified by equation (IV.1) [28]:

$$\Delta \boldsymbol{W} = \frac{\boldsymbol{B} - \boldsymbol{W}}{2} \approx \frac{1}{2} \frac{\boldsymbol{S} * \boldsymbol{G}}{\boldsymbol{D}} \tag{IV.1}$$

This extension is proportional to the gap. With the aim of recovering nominal dimensions, the correction of this loss of resolution has been the purpose of the work exposed in this section. As an example, a gap value of G = 10 µm results in a 100 nm blurring extension ΔW.

All experiments were made with a deposition system with long source-target distance (1 m). This provides two advantages: blurring is reduced [refer to eq.(IV.1), as D increases] and lateral offsets (X value) can be neglected since D is much bigger than any other dimension.

In initial experiments, several Si wafers were patterned with SiO_2 pillars (on which stencils lean on), whose thickness varies in the 1-10 µm range from one wafer to another.

Subsequent experimental tests with predefined gaps show a resulting pattern that is a combination of:

- a well-defined *main pattern* whose flanks are abrupt (see Figure 13) and which size can be determined by eq. (IV.1).
- a surrounding thin metal layer or halo caused by surface migration, whose extension is material dependent.

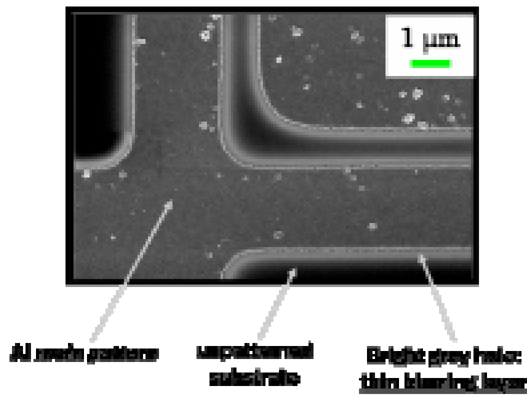

Figure 13. Scanning Electron Microscope (SEM) image of a main pattern with well defined contours and surrounding halo

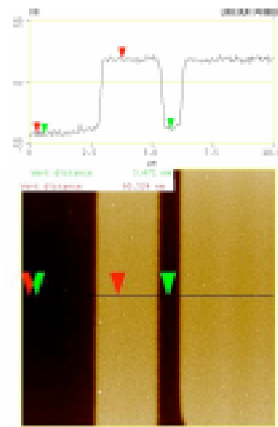

Figure 14. Atomic Force Microscope (AFM) picture: pattern profile with abrupt flanks

The thin Al halo is less than 5 nm thick, i.e. much thinner than the *main pattern* thickness (more than 50 nm). However, it is strong enough to sustain subsequent reactive ion etchings of SiO_2 and Si. This fact represents a major problem when a pattern contains features like small gaps because a proper trench formation is impeded (see Figure 15).

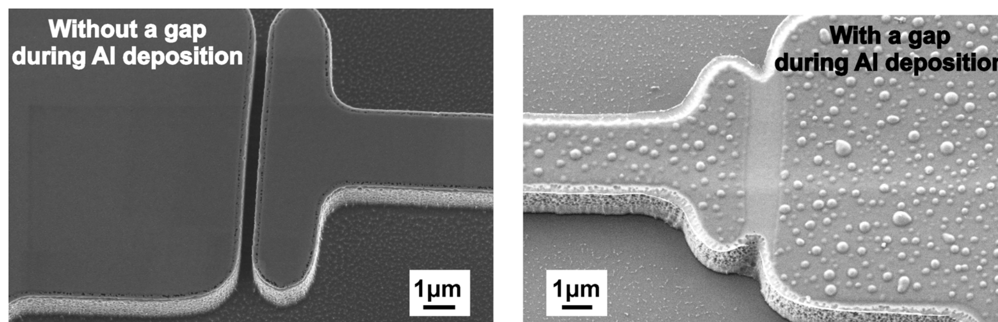

Figure 15. SEM pictures of nanostencil-deposited Al patterns transferred by RIE to silicon.

The *main pattern* exhibits several characteristics. First, we confirm that its thickness corresponds to the nominal deposited thickness (in our case from 50 nm up to 80 nm). Second, it has well-defined contours with abrupt flanks surrounded by a thin layer (a halo). This is a very relevant point that differs much from other materials, like Cu, that exhibit a progressive profile [5] in which there is no clear distinction between the blurring and the *main pattern*. Third, a good correspondence has been observed between its dimensions and the stencil aperture size: if the halo extension is disregarded, its dimensions are in agreement with eq.(IV.1).

As an additional remark, it is important to emphasize the major influence of the nanostencil structure on the blurring extension and its profile. All the previous observations are valid for lithography steps carried out with clean unstabilized nanostencils or stabilized nanostencils (with corrugated membranes) that do not deflect when material is deposited on them [33]. On the contrary, reused (already metal-coated) unstabilized stencils bend and therefore another model is required. In this case, the membrane progressively deflects locally around the apertures during

metal deposition because of an increasing stress (depending on the aperture shape, it is more or less sensitive). This means that the membrane aperture size and the gap are constantly increasing and varying, and consequently the pattern profile will be different.

CORRECTIVE ETCHING PRINCIPLE AND PROCESS DETAILS [31]

To overcome the loss of nominal dimensions due to blurring effect, in particular for the case of patterns with small gaps (i.e. trench definition), a corrective etching has been developed to recover nominal pattern dimensions. We have found that by performing a uniform controlled etching of a few nanometers of the deposited layer, its thickness is uniformly decreased all over the sample. Then, the characteristic thin blurring layer is eliminated (see Figure 16) because the blurring layer is much thinner than the *main pattern*.

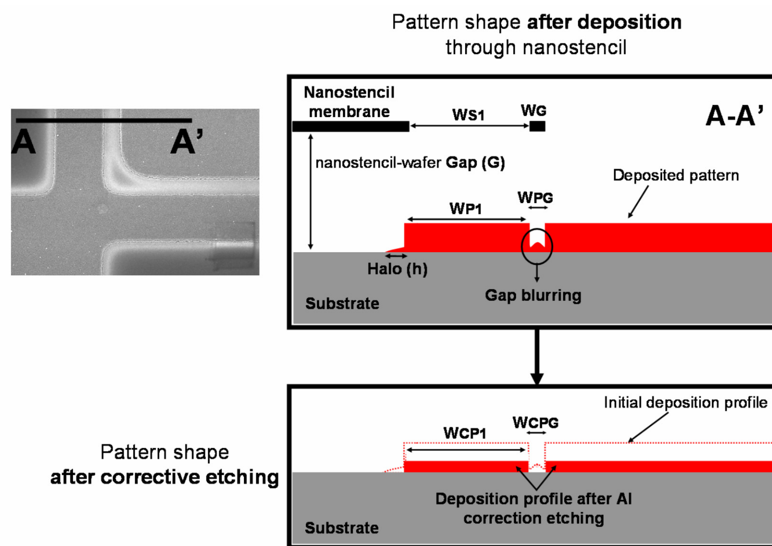

Figure 16. Sequential scheme for blurring correction

Two processes of controlled dry etching of Al were successfully developed: one recipe has been adapted to QUAD DRYTEK systems (LAM RESEARCH CORP., Fremont, CA) (anti-blurring recipe nº1, *AB1*), in order to be applied at CNM. The other has been adapted to STS MULTIPLEX ICP systems (*AB2*) in order to be applied at EPFL. Some initial unsuccessful tests of wet etching made us turn to dry etching processes for reasons of uniformity, repeatability and controllability.

Initial experiments were performed on chip-sized samples (silicon substrate with 100 nm thick thermal oxide grown on top) on which 70 nm thick Al patterns were deposited by nSL. Chip-sized nanostencils were used for testing in the QUAD DRYTEK system and therefore the *AB1* recipe was optimized for chip-sized samples (a recipe for whole wafer would also be feasible on this equipment). A special carrier wafer with equal Al/resist distribution is required to ensure etching uniformity over the chip. *AB1* is based on two steps: first, the thin native Al oxide layer (Al_2O_3) [38], which is resistant to many wet etchers, is removed under the following conditions: BCl_3 flow of 50 sccm, chamber pressure 325 mT, radio frequency (RF) power 125 W, chamber temperature 55°C. Then, chlorine chemistry is used to etch the precleaned thin Al layer. Assuming a 25 nm thick Al etching as a minimal target, we use a mixture of Cl_2 (as Al etcher):

BCl_3 (to reduce the etch rate by neutralizing H_2O): N_2 (for better uniformity and low etch rate) with respective flows of 3:12:80 sccm (rest of conditions: 325 mTorr, 125 W, 55°C). The resulting etch rate is approximately 100 nm/min.

In the STS MULTIPLEX system (Inductive Coupling Plasma), a recipe (*AB2*) was specifically tuned for wafer-sized samples. Due to different characteristics between both systems, another type of recipe was optimized, based on a single step of BCl_3 with a 10 sccm flow at 3 mTorr. Plate power and RF power are respectively 30 W and 600 W. Just like in the recipe for QUAD DRYTEK systems, BCl_3 first removes native Al oxide but then its own action does not require any additional gas to etch Al itself. With this configuration, a sufficiently low etch rate around 100 nm/min is obtained and *AB2* provides excellent reproducibility and uniformity at wafer scale.

Using any of these recipes, the pattern widening is corrected as illustrated in the SEM images of Figure 17.

On left images, the bright halo surrounding the Al *main pattern* corresponds to the blurring. In the top row, blurring was not corrected and consequently trench definition is failed after RIE of silicon. In the second (chip-sized samples with a well-known step and corrected with *AB1*) and third row (whole 100 mm CMOS wafer corrected with *AB2*), a successful implementation of the recipes is demonstrated. In both kinds of samples, the bright halo disappears after the corrective etching of Al, and therefore a trench is successfully fabricated after the subsequent RIE of Si.

In Table IV - 2, we summarize the evolution of the pattern dimensions along the process sequence (in annex A7.4, more data are provided on pattern transfer and blurring extension): from the initial aperture size into the nanostencil until the final dimension of the pattern after the corrective etching. Deviation of final pattern dimensions with respect to the dimensions in the stencil is less than 10% in most of the cases. A perfect uniformity of the etching is verified at chip and wafer level.

Device location		Dimensions in stencil (nm)	Dimensions on patterned sample (nm)			
			Deposited pattern	Blurring (2·*h*)	Corrected pattern	Blurring (2·*h*)
Location 1	Beam	310 (*WS1*)	236 (*WP1*)	280 Unformed trench	267 (*WCP1*)	0 Opened trench
	Space between two patterns	775 (*WG*)	856 (*WPG*)		813 (*WCPG*)	
Location 2	Beam	295 (*WS1*)	291 (*WP1*)	500 Unformed trench	323 (*WCP1*)	0 Opened trench
	Space between two patterns	750 (*WG*)	788 (*WPG*)		769 (*WCPG*)	

Table IV - 2. Patterns transfer data: patterns dimensions evolution along the process sequence. Refer to Figure 16 for the meaning of each dimension. Locations 1 and 2 are two different locations separated by several centimeters over a 100 mm wafer.

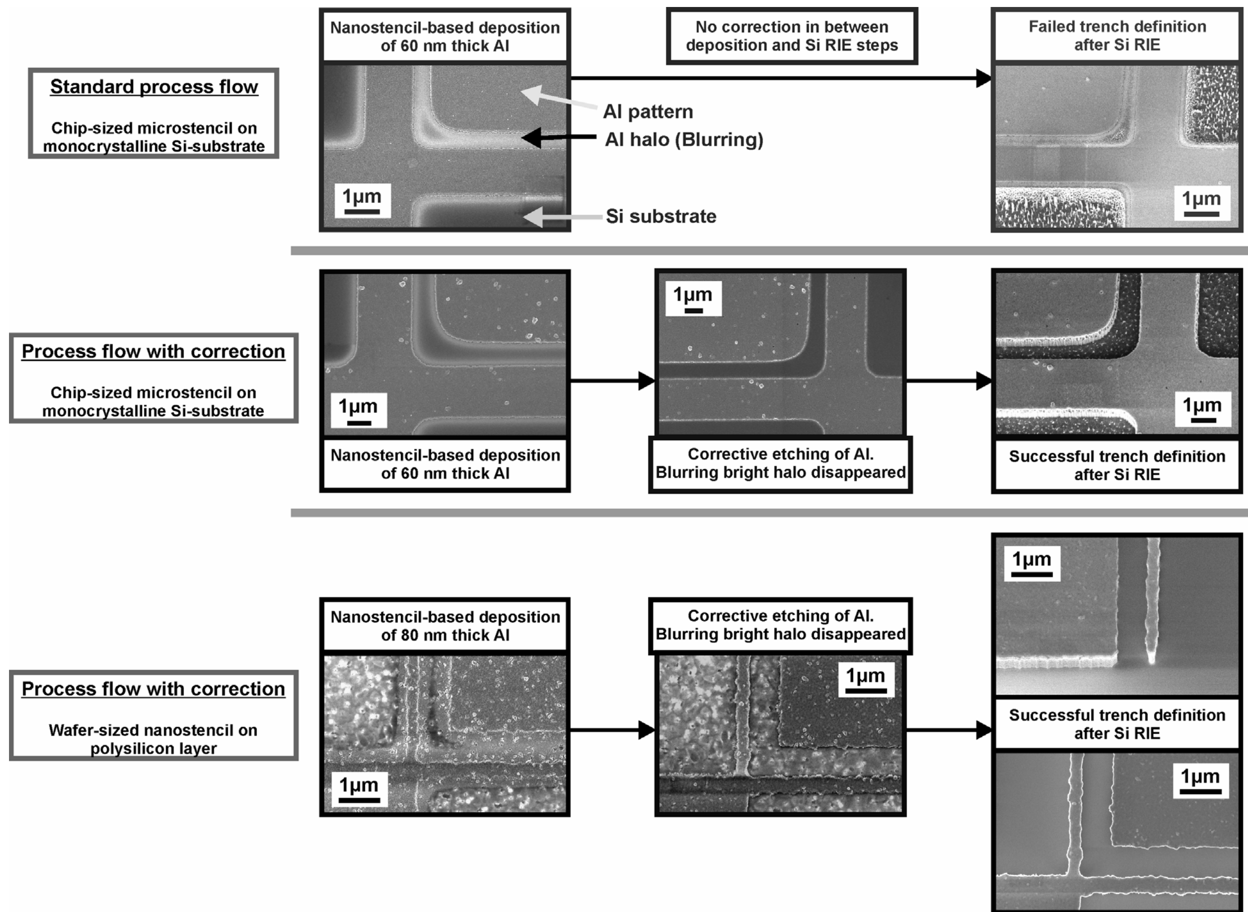

Figure 17. Visual comparison without/with blurring correction

II.2.c. Dummy wafers

It was not cost-effective to optimize the entire post-processing technology using CMOS wafers. This is why two kinds of dummy wafers were designed and fabricated in order to make various types of test: some for testing the successive post-processing steps, some others for the study and the correction of nSL related issues, like alignment or blurring.

DUMMY WAFERS OF TYPE 1 ("*DUMMIES 1*")

Their function is to help adjusting recipes of various dry etchings:

- dry etching in one step of two layers: *passivation* + *interlevel oxide*.

  This etch makes an aperture in those materials in order to give access to nanodevices integration areas.
- dry etching to remove *poly1* layer (that protects the structural layer *poly0*)
- dry etching to remove the *gate oxide* separating *poly1* and *poly0*, with Al patterns as etch masks (deposited by nSL).
- dry etching of *poly0* layer (resonators structural layer), also with Al patterns as etch masks.

Moreover, they should help testing the alignment between CMOS and nanostencil wafers. In parallel, the blurring that will affect the CMOS wafers can initially be precisely estimated (because CMOS and dummy wafers have an identical topography so that their nanostencil-wafer gap is comparable). The fabrication process of dummies 1 in detailed in annex A7.2

LIST OF TESTS MADE WITH DUMMIES 1: their structural composition and their topography allow performing a series of optimization tests detailed hereafter:

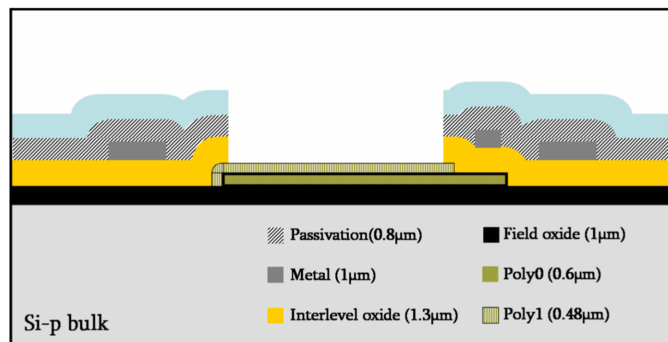

Test nº1: Successive dry etchings of *passivation* and *interlevel oxide* layers.

- photoresist as an etch mask
- succession of two recipes for both layers (Si_3N_4 oriented, then SiO_2 oriented recipes). Selectivity SiO_2/Si required.

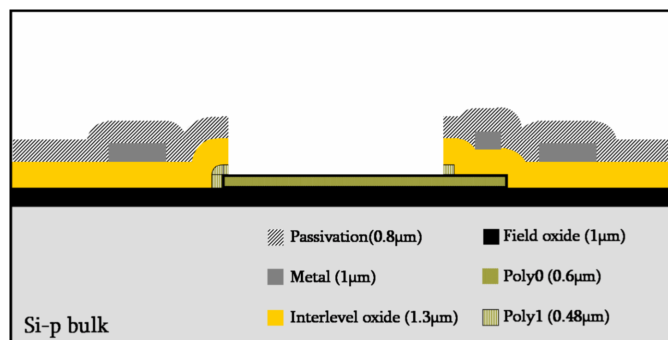

Test nº2: Dry etching of *poly1* with *passivation* and *interlevel oxide* layers as etch mask (no photoresist during this etch, selectivity Si/SiO_2 required)

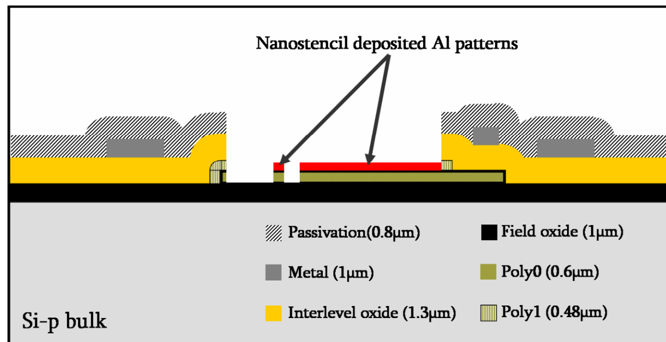

Test nº3: Dry etching of *gate oxide* with Al patterns deposited by nSL as etch mask. Selectivity SiO_2/Si required.

Test nº4: Dry etching of *poly0* with Al patterns deposited by nSL as same etch mask. Selectivity Si/dielectrics required.

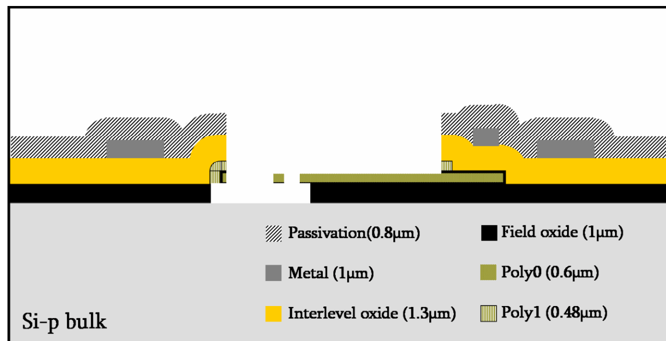

Test nº5: Development of the release process of wide and narrow nano/micromechanical resonators (etch time more or less long).

DUMMY WAFERS OF TYPE 2 (“*DUMMIES 2*”)

Their function is to study the blurring extension (ΔW, see Figure 12) as a function of a known gap. For this purpose, SiO_2 steps of several well-controlled heights are made. By measuring ΔW at several sites of the wafers (center, borders), information on clamping uniformity will be extracted as well. Their fabrication process in detailed in annex A7.2.

II.3. Post-processing of pre-fabricated CMOS wafers based on nSL

Hereafter, we present a detailed description of the process flow that leads to the complete fabrication of nano/micromechanical resonators on CMOS. Our approach consists in post-processing prefabricated standard CMOS wafers using nanostencil lithography (nSL) as nanopatterning technique of the nanodevices.

II.3.a. *poly1* removal

After CMOS fabrication is completed, pads and integration areas are the single zones in which the passivation layer is opened. To access the structural layer (*poly0*), it is necessary to remove entirely the 480 nm thick *poly1* layer until arriving to the 70 nm thick thin oxide grown on *poly0*. (*poly1* had a function of protecting *poly0* during CMOS fabrication).

The removal is achieved by performing a RIE of *poly1* that must combine high selectivity with respect to Al (contact pads must not be damaged) and to dielectrics (SiO_2 and SiN, the passivation must not be damaged while the underlying thin oxide must remain intact, otherwise *poly0* may start to be etched). The uniformity at wafer scale is another key feature of the recipe.

For an easier detection of the etching end point, several extended test zones (400*400 μm^2) were included in the chip layout. They have such a profile: bulk silicon + gate oxide (70 nm) + *poly1* (480 nm). Their big size allows utilizing an ellipsometric technique, based on a large laser spot, that monitors the etching by measuring the remaining *poly1* thickness.

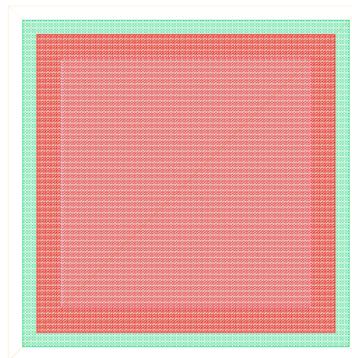

Figure 18. Layout of the test structure of *poly1* etching (400*400μm^2)
[green: bulk Si area; red: *poly1* area; violet: aperture in passivation]

PROCESS DETAILS:

System: ICP Alcatel A601E (recipe *Nano1 cont*) at CNM. The recipe is continuous and all gases are injected simultaneously.
t: 1min 20s
C_4F_8: 45 sccm
SF_6: 35 sccm
Pressure: 2.10^{-2} mbar
ICP Power: 1000 W
Plate power: 5 W

II.3.b. Alignment

It was performed at EPFL on a SÜSS MICROTEC MA/BA6 (mask aligner/bond aligner) system with a modified custom chuck developed by the same company in the framework of NaPa..

GENERAL ISSUES ALIGNMENT STENCIL TO CMOS

The microscope for topside alignment can be used in Bond Aligner-mode. In our experiments we have lowered the alignment gap to 20 µm (15 µm alignment gap shows a mechanical friction between stencil and substrate). The topography of the CMOS and the tolerances in the thickness and curvature of both stencil and substrate may make it difficult to align due to the depth of focus of the objectives.

ALIGNMENT RESULTS

Two CMOS substrates (CMOS11 and CMOS14) and one stencil (ST2-2182) were used for alignment experiments in which the misalignment was measured and analyzed based on Al patterns deposited by nSL. For both CMOS wafers, the obtained results were very similar. Therefore, we only present the results of CMOS wafer nº11.

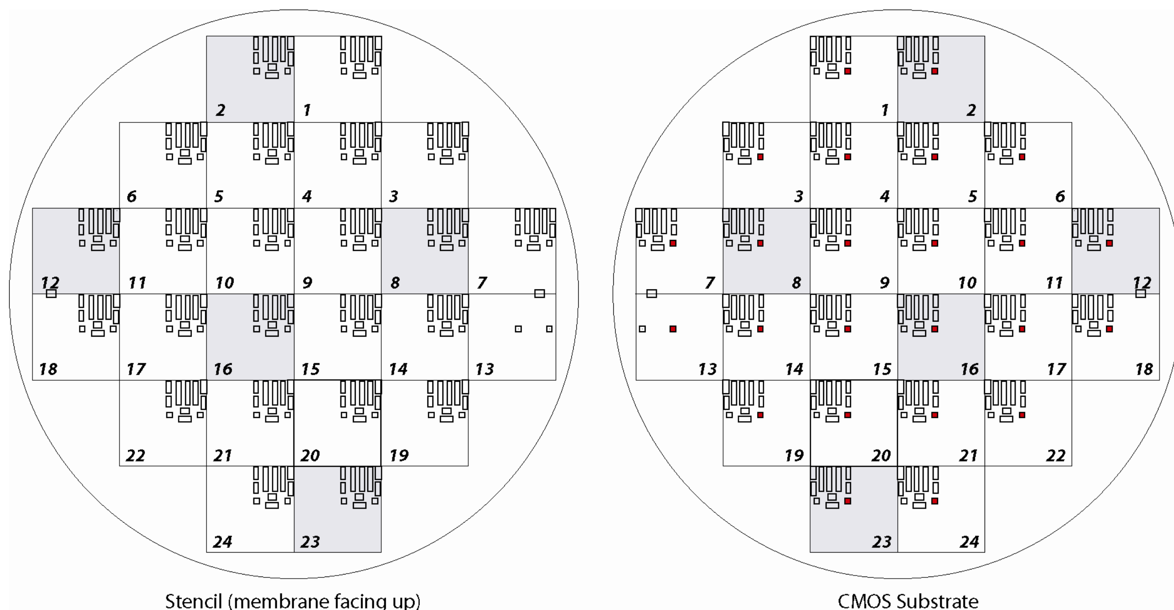

Figure 19. Stencil and CMOS design showing exposure fields and structure areas. The alignment markers in the 24 chips were measured.

In order to measure the misalignment between stencil and CMOS, the alignment marks on the stencil are considered accurate since they were patterned by DUV with a precision of 20 nm (ASML specifications). On the opposite, we have observed a scaling error between each CMOS chips, materialized by a linear increase of misalignment within a row or a column of chips..

The measurements of all 24 chips were performed on an optical microscope. Several of those fields were measured using a SEM. SEM measurements showed that optical microscope measurements are sufficiently accurate.

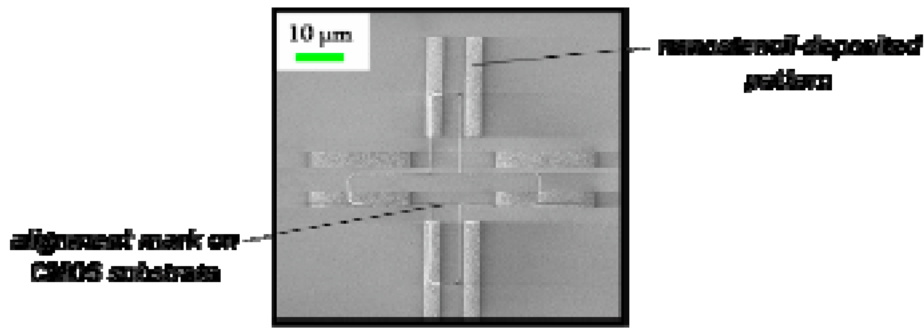

Figure 20. Example of an alignment mark used in stencil alignment. The cross marker is present on the CMOS substrate. The 8 lines are Al patterns deposited by nSL.

RESULTS OF ALIGNMENT OF ST2-2182 TO CMOS11

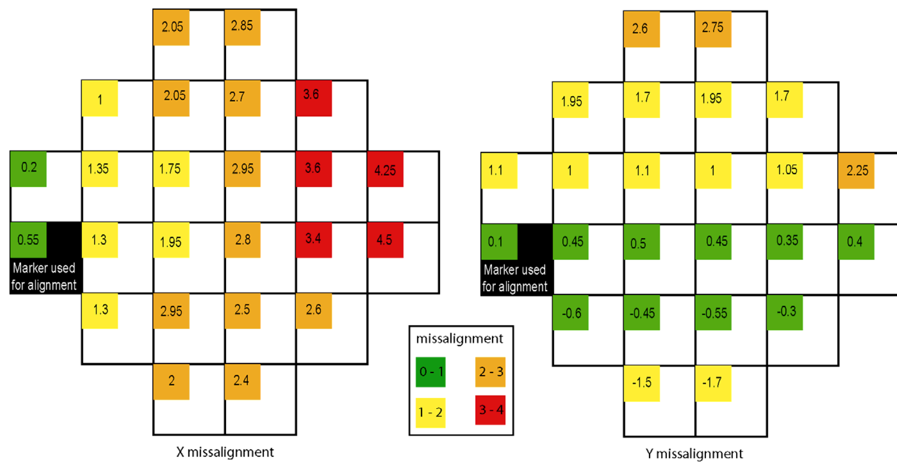

Figure 21. Misalignment results (in microns), measured with an optical microscope. The black field was used to align both X and Y, taken as a reference. The image shows an increase in misalignment radiating from the initial alignment marks.

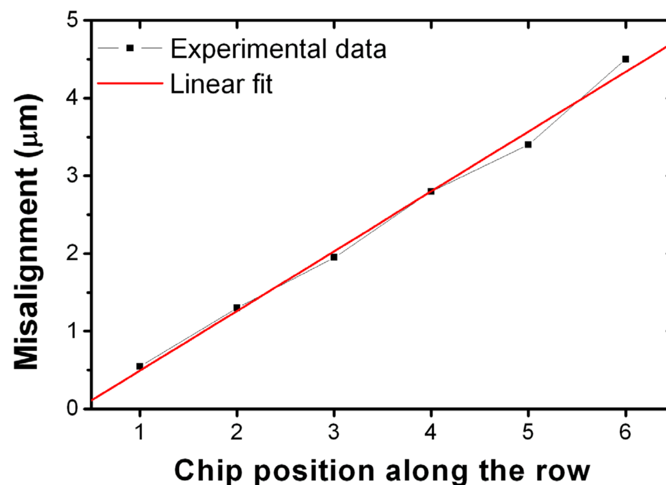

Figure 22. Graph showing a linear increase in misalignment in x direction for chips 13 through 18 (see Figure 19), second row.

From the linear fit of Figure 22 and the observed very linear trend of misalignment error measured along a row of chip (the same was observed along any other row and any column), we estimate around 0.8 µm per chip the scaling error of CNM UV stepper. Further experiments for compensating this error are planned to be performed.

OVERALL ALIGNMENT RESULTS

Both alignments were successful and considering only the reference chip used for the first alignment, an accuracy below 1 µm is obtained:

- for the first wafer, the misalignment was ΔX=0.55 µm and ΔY=0.1 µm at the alignment site
- for the second wafer, the misalignment was ΔX=0.1 µm and ΔY=-0.85 µm at the alignment site

These alignment results were achieved after evaporation what means that the alignment stays within the tolerance targets during transportation and fixing of the chuck inside the evaporator.

II.3.c. Al deposition

The stencil-substrate chuck must be transported to the deposition system (LEYBOLD-OPTICS LAB 600H at EPFL) for performing a deposition of Al through the apertures of the full-wafer nanostencil. The technique employed is electron beam evaporation. Around 10^{-7} mbar, the Al crucible is bombarded by a high energy electron beam proceeding from a heated tungsten filament. Only the surface of the crucible is melt and evaporates; for this reason no cross contamination from the walls is generated and high purity Al is deposited. The high source-substrate distance (1 m) of the chamber contributed to minimize dispersive effects that lead to pattern widening [see eq.(IV.1)].

A 90 nm thick Al layer has been deposited on each wafer. The deposited thickness has been measured by in-situ quartz-crystal microbalances and subsequently by a mechanical profilometer indicating 80-85 nm.

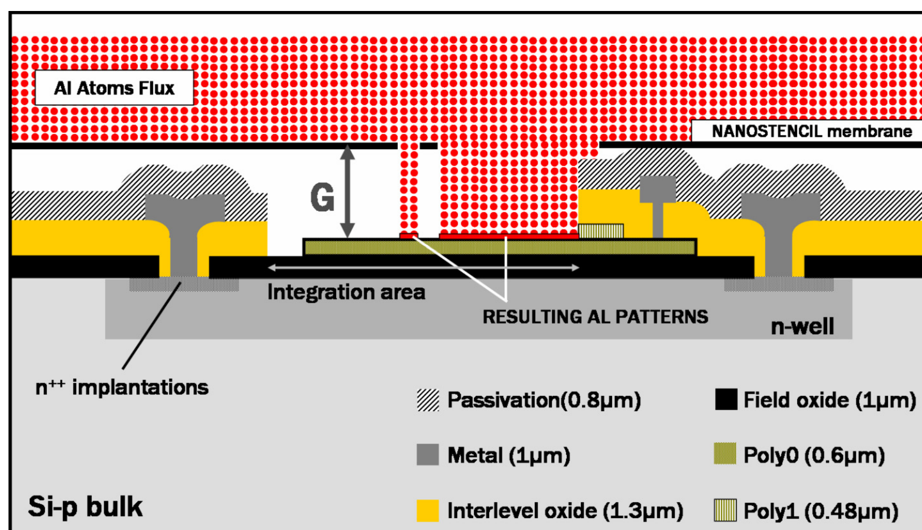

Figure 23. Al deposition through nanostencil onto a CMOS wafer

II.3.d. Blurring correction

As explained in section II.2.b, because of the so-called *blurring effect*, Al patterns deposited by nSL are inherently more or less distorted and widened, with respect to the nominal dimensions defined by the dimensions of stencil apertures. They need to be corrected for improving their definition. This "correction" is based on a dry etching that uniformly decreases at wafer scale the thickness of the Al patterns and therefore removes the halo caused by the *blurring effect*. Hereafter are given the process details of the etching performed at EPFL.

PROCESS DETAILS OF AL ETCH:

System: ICP STS Multiplex (recipe *Al-slow*)
t: 20 s
BCl_3: 10sccm
Pressure: 3 mTorr
ICP Power: 600 W
Plate power: 30 W
Nominal etching speed: 100 nm/min at RT

II.3.e. Pattern transfer and release

As aforementioned, the Al patterns were deposited onto a thin oxide (70 nm) that initially separated *poly0* from *poly1*. Once deposition and correction are completed, the Al patterns must be transferred first to the thin oxide (70 nm thick) and second to *poly0* (600 nm thick). At this step, the polysilicon nanomechanical devices get their 3D shape. Hereafter are given the details of the two successive etching steps performed at EPFL.

PATTERN TRANSFER (TWO ETCHINGS) WITH CORRECTED AL MASK

(1) RIE OF THE THIN SiO_2 (70 NM THICK)

System: AMS 200 Adixen (recipe SiO_2 PR 1:1)
t: 25 s
C_4F_8: 15 sccm
Pressure: 8.10^{-3} mbar
ICP Power: 1800 W
Plate power: 120 W (about 100V)
Nominal etching speed: 280 nm/min at RT

(2) RIE OF *POLY0*

System: AMS 200 Adixen (recipe Si opto)
t: 50 s
C_4F_8: 40 sccm
SF_6: 50 sccm
Pressure: 3.10^{-2} mbar
ICP Power: 1500 W
Plate power: 15 W
Nominal etching speed: 1200 nm/min at RT

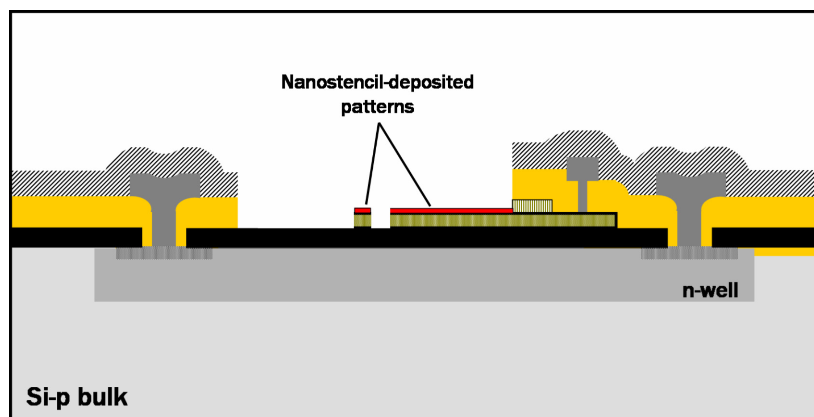

Figure 24. Pattern transfer to SiO_2 and polySi by successive RIE with corrected Al patterns as a mask

WAFER DICING (PERFORMED AT CNM)

The wafers are diced into individual chips at this step of the process (before resonators release) because already released mechanical devices would be more susceptible to break during dicing. A standard photoresist is roughly coated over the wafer with a paintbrush before dicing. This operation protects the wafer surface from the particles arising from dicing (then the resist is simply removed in acetone).

RELEASE PROCESS OF NANO/MICROMECHANICAL RESONATORS (PERFORMED AT CNM)

The last main step consists in releasing the nanomechanical devices relying on a photolithography process that makes apertures in the photoresist only around the resonators so that the rest of the chip (i.e. CMOS circuitry) remains protected. The apertures have a rectangular shape and are centered on each resonator. Their dimensions depend on each resonator: a minimum 10 μm distance between every point of the resonator and the aperture border has been respected.

We have developed two different processes for the subsequent local wet etching (see Figure 25) according to the size of resonator. Both alternatives have demonstrated reproducibility and reliable release. It must be noticed that the wet etching step has two functions: (i) it releases the resonators and (ii) it removes the remaining layers, Al mask and thin gate oxide, that lean on the polysilicon structural layer.

For narrow devices (width in the micron/submicron range), like in-plane vibrating cantilevers, short etching times are sufficient and the resist withstands the aggressiveness of the solution.

RELEASE PROCESS OF CANTILEVER (SHORT RELEASE ETCHING TIMES)

- **Step 1.** Standard photoresist (HPIR 6512) patterning
  Dehydration. 1h at 200°C
  Spinner. 3500 rpm, 1500 rpm/s, 45s
  Soft-bake. 15 min at 100°C
  Exposure: hard-contact, 15 s
  Development: 30s + rinsing in water
  Hard bake: 20 min at 100°C, ramp until 175°C, then 30 min at 175°C then soft descent until room temperature (~30 min)

- **Step 2.** Release wet etching
  SiOetch: 4 min (for 300 nm wide devices)
  Drying with a critical point dryer to avoid sticking

- **Step 3.** Resist stripping
  Resist stripping based on O_2 plasma in a TEPLA machine.

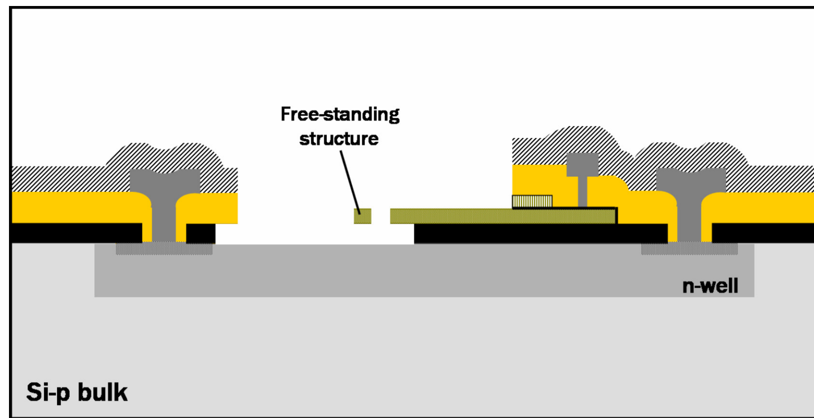

Figure 25. Released nanocantilever after photolithography and wet etching in BHF

For larger devices (width in the order of several microns), like quad-beams, long etching times are required but after a certain time the resist does not withstand anymore and strips.

Consequently, we use an alternative process whereby we first coat and pattern (with standard UV lithography) a SU8 layer (acting as negative resist) on top of the CMOS substrate. SU8 is very resistant to solutions based on HF. Then, to make this process even more reliable, we coat on top of this structured SU8 layer a standard photoresist and follow the same procedure as for cantilevers: as a consequence, the CMOS chip has a double protection during the HF etching.

RELEASE PROCESS OF QUAD-BEAMS RESONATORS (LONG RELEASE ETCHING TIMES)

- **Step 1.** SU8 deposition and patterning
  Cleaning in acetone, IPA and water
  Dehydration. 1h at 200°C
  Spinner. 3000 rpm, 1500 rpm/s, 30s (to obtain a ~ 5µm thick SU8 layer)
  Soft-bake. ramp from 65°C until 95°C, then 10 min at 95°C
  Exposure: soft-contact, 12s
  Post-exposure bake: ramp from 65°C until 95°C, then 20min at 95°C
  Development: 1 day after, 6 min + IPA.

- **Step 2.** Standard photoresist (HPIR 6512) patterning on top of SU8
  identical to step 1 for cantilevers

- **Step 3.** Release wet etching
  Objective: wet etch locally, in a controllable way, the sacrificial field oxide layer in order to release the mechanical structures
  Etchant: "SE34" solution. HF49% : NH4F [buffered] : CH3COOH [weak acid] (1:10:5 in volume)
  Etching velocity: ~ 5 µm/hour. This value tends to decrease with time.
  - SE34 20 min + annealing 30 min 125-130ºC + SE34 20 min (for 6.2 µm wide devices)
  - Drying with a critical point dryer to avoid sticking

- **Step 4.** Resists stripping
  Resist stripping based on O_2 plasma in a TEPLA machine.
  SU8 is partially stripped although the standard photoresist is completely removed

II.3.f. Test of CMOS compatibility of nSL

After successfully demonstrating the potential of a CMOS post-processing technology based on nSL, it has been analyzed at CNM if specific processes related to nSL (evaporation and blurring correction) could eventually modify the performance of CMOS circuitry. It has been proven that electron beam lithography (EBL) degrades CMOS transistors performance [35] for acceleration voltages superior to 15 keV: in particular, threshold voltage and transconductance properties seem to be affected. In this context, it was important to demonstrate that nSL, beyond its great interest in terms of technology (clean, parallel, high-resolution, etc…), is a safe tool for CMOS circuitry post-processing in the sense that it does not modify its performance.

To carry out a comparison of the performances before and after CMOS post-processing, a simple CMOS-based voltage amplifier was electrically characterized: its static and dynamic response did not exhibit any relevant evolution.

In parallel, characteristic parameters of CNM CMOS technology, such as transistor threshold voltage, leakage current, square and contact resistances have been measured by means of specifically designed test structures: no substantial changes have been observed after post-processing, as it is shown in Figure 26:

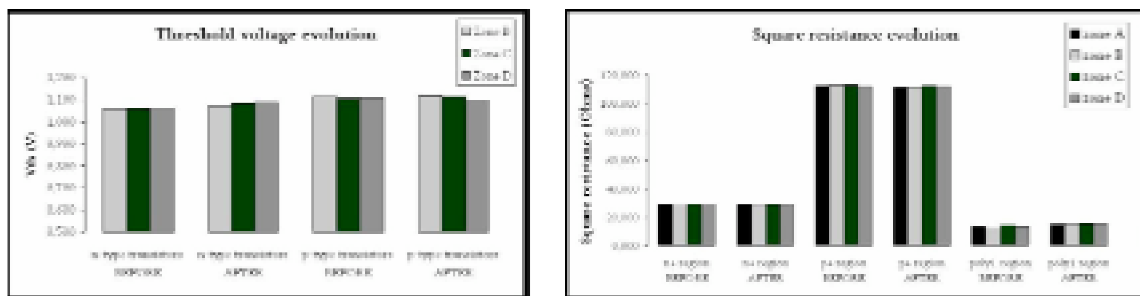

Figure 26. Evolution of characteristic parameters before and after the entire nanostencil process (Al evaporation and subsequent corrective dry etching): measurements of threshold voltage (left) and square resistance (right) of MOS transistors (test structures)

We have not found any relevant difference in the electrical performance of the circuits before and after nSL, neither for the test circuits located far from the integration areas nor for the readout circuits located besides the integration areas and connected to them. This means that any spatial proximity between nanomechanical device patterned by nSL and CMOS circuitry has no incidence on its performance and therefore a high density of integration is affordable with this nanopatterning technique.

FINAL RESULTS OF POST-PROCESSING

Full-wafer nanostencil lithography (nSL) has been applied to define 200 nm scale Si nanomechanical devices (resonators) monolithically integrated into CMOS circuits, using one single metal evaporation (nSL step), pattern transfer to Si by RIE and subsequent release etch of the sacrificial layer. In this way, we have achieved the simultaneous nanopatterning of ~2000 nanodevices on entire 100 mm pre-patterned standard CMOS substrates (see Figure 27). In each wafer (in total three wafers were patterned), there are 24 CMOS/NEMS chips (7.5*7.5 mm^2) containing each one 78 resonators.

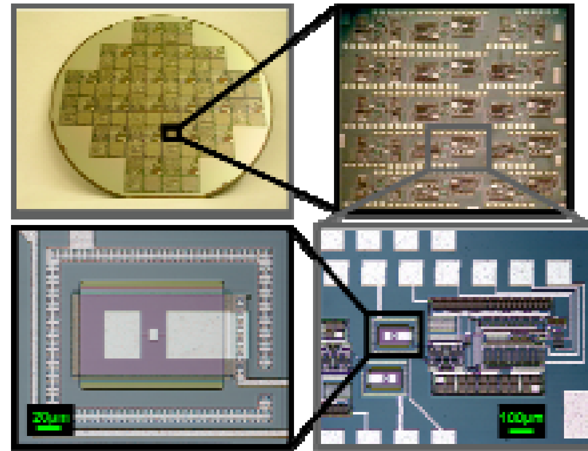

Figure 27. Full CMOS wafer (100 mm) with ~2000 nanomechanical resonators patterned by nanostencil lithography and monolithically integrated with CMOS readout circuits.

Several types of NEMS resonators fully integrated with readout CMOS circuitry were fabricated (see Figure 28): cantilevers, quad-beams and paddles.

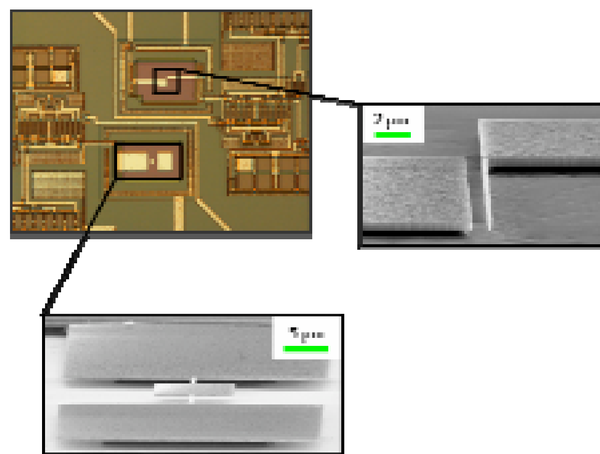

Figure 28. Examples of two types of 600 nm thick polysilicon resonators integrated with CMOS circuitry. A cantilever beam is depicted on the right: it has a width of 200 nm and the gap separating from its electrode is 800 nm wide. It is 14 μm long and 600 nm thick. The bottom resonator is a torsional paddle.

III. Fabrication of nano/micromechanical resonators on CMOS by electron-beam lithography (eBL)

The approach we have followed to fabricate nanodevices on pre-fabricated standard CMOS wafers by eBL is absolutely similar to the nSL based process: it differs only about the lithography technique. This process can be entirely performed in CNM clean room.

Compared to nanostencil lithography eBL is slow and serial. However the development of such a technology is a great opportunity to be able to fabricate in-house new prototypes within a short timeframe. The lithography step is performed with a relatively low voltage in order not to degrade the performance of the circuitry.

All the process details of the entire post-processing based on eBL are given in annex A7.3.

Conclusion of chapter 4

The potential of nanostencil lithography as a parallel, straightforward and CMOS compatible patterning technique to define devices on CMOS at the 200 nm scale has been demonstrated. Further decreasing the resolution below 50 nm is on progress.

Three 100 mm CMOS wafers (each one containing 24 chips) were post-processed according to this technique. This resulted in the complete fabrication of about 2000 resonators, per wafer, monolithically integrated with a CMOS readout circuitry.

In terms of technology, two critical issues have been solved: alignment full-wafer nanostencil/CMOS wafer at 100 mm wafer scale, and pattern blurring effect correction for enhanced resolution.

In terms of device operation, it has been demonstrated that a post-processing of CMOS wafers based on nanostencil lithography does not affect the circuitry performance. The work reported in this thesis represents the first time that an emerging nanolithography technique has been used to pattern multiple NEMS/MEMS devices on a whole CMOS wafer in a parallel and relatively low-cost approach.

The same strategy could be extended to other examples of nanodevices, such as single electron transistors (SETs) on CMOS [39], for which there is at present no affordable technological process that fulfill the requirements of high resolution processing at full wafer scale and CMOS compatibility.

Inspiring from this approach of integration, an almost identical post-processing technology based on electron beam lithography has also been developed to be able to fabricate new prototypes of nanodevices on CMOS within short timeframes.

Bibliographical references

1. Arcamone, J., M.A.F.v.d. Boogaart, F. Serra-Graells, S. Hansen, J. Brugger, F. Torres, G. Abadal, N. Barniol, and F. Pérez-Murano
Full-wafer integration of NEMS on CMOS by nanostencil lithography
in the proceedings of the *IEEE IEDM*. 2006. San Francisco (USA).

2. Verd, J., G. Abadal, J. Teva, M.V. Gaudo, A. Uranga, X. Borrise, F. Campabadal, J. Esteve, E.F. Costa, F. Perez-Murano, Z.J. Davis, E. Forsen, A. Boisen, and N. Barniol
Design, fabrication, and characterization of a submicroelectromechanical resonator with monolithically integrated CMOS readout circuit
IEEE Journal of Microelectromechanical Systems, 2005. **14**(3): p. 508-519.

3. De Poortere, E.P., H.L. Stormer, L.M. Huang, S.J. Wind, S. O'Brien, M. Huang, and J. Hone
1-to 2-nm-wide nanogaps fabricated with single-walled carbon nanotube shadow masks
Journal of Vacuum Science & Technology B, 2006. **24**(6): p. 3213-3216.

4. De Poortere, E.P., H.L. Stormer, L.M. Huang, S.J. Wind, S. O'Brien, M. Huang, and J. Hone
Single-walled carbon nanotubes as shadow masks for nanogap fabrication
Applied Physics Letters, 2006. **88**(14).

5. van den Boogaart, M.A.F.
Stencil lithography: an ancient technique for advanced micro- and nanopatterning
Hartung-Gorre Verlag ed, Series in Microsystems, Vol. 20, 2006, Konstanz.

6. van den Boogaart, M.A.F., G.M. Kim, R. Pellens, J.P. van den Heuvel, and J. Brugger
Deep-ultraviolet-microelectromechanicaI systems stencils for high-throughput resistless. patterning of mesoscopic structures
Journal of Vacuum Science & Technology B, 2004. **22**(6): p. 3174-3177.

7. Ludwig, A., J. Cao, J. Brugger, and I. Takeuchi
MEMS tools for combinatorial materials processing and high-throughput characterization
Measurement Science & Technology, 2005. **16**(1): p. 111-118.

8. Takahashi, R., H. Kubota, M. Murakami, Y. Yamamoto, Y. Matsumoto, and H. Koinuma
Design of combinatorial shadow masks for complete ternary-phase diagramming of solid state materials
Journal of Combinatorial Chemistry, 2004. **6**(1): p. 50-53.

9. Zhou, Y.X. and A.T. Johnson
Simple fabrication of molecular circuits by shadow mask evaporation
Nano Letters, 2003. **3**(10): p. 1371-1374.

10. Tian, P.F., P.E. Burrows, and S.R. Forrest
Photolithographic patterning of vacuum-deposited organic light emitting devices
Applied Physics Letters, 1997. **71**(22): p. 3197-3199.

11. Egger, S., A. Ilie, Y.T. Fu, J. Chongsathien, D.J. Kang, and M.E. Welland
Dynamic shadow mask technique: A universal tool for nanoscience
Nano Letters, 2005. **5**(1): p. 15-20.

12. Guo, H.M., D. Martrou, T. Zambelli, J. Polesel-Maris, A. Piednoir, E. Dujardin, S. Gauthier, M.A.F. van den Boogaart, L.M. Doeswijk, and J. Brugger
Nanostenciling for fabrication and interconnection of nanopatterns and microelectrodes
Applied Physics Letters, 2007. **90**(9).

13. Gross, L., R.R. Schlittler, G. Meyer, A. Vanhaverbeke, and R. Allenspach
Fabrication of ultrathin magnetic structures by nanostencil lithography in dynamic mode
Applied Physics Letters, 2007. **90**(9).

14. Racz, Z., J.L. He, S. Srinivasan, W. Zhao, A. Seabaugh, K.P. Han, P. Ruchhoeft, and J. Wolfe
Nanofabrication using nanotranslated stencil masks and lift off
Journal of Vacuum Science & Technology B, 2004. **22**(1): p. 74-76.

15. Kolbel, M., R.W. Tjerkstra, J. Brugger, C.J.M. van Rijn, W. Nijdam, J. Huskens, and D.N. Reinhoudt
Shadow-mask evaporation through monolayer-modified nanostencils
Nano Letters, 2002. **2**(12): p. 1339-1343.

16. Brugger, J., J.W. Berenschot, S. Kuiper, W. Nijdam, B. Otter, and M. Elwenspoek
Resistless patterning of sub-micron structures by evaporation through nanostencils
Microelectronic Engineering, 2000. **53**(1-4): p. 403-405.

17. Kaminsky, G.
Noncontaminating Si-Based Shadow Masks for Mbe
Journal of Vacuum Science & Technology B, 1985. **3**(2): p. 741-742.

18. Kim, G.M., M.A.F. van den Boogaart, and J. Brugger
Fabrication and application of a full wafer size micro/nanostencil for multiple length-scale surface patterning
Microelectronic Engineering, 2003. **67-8**: p. 609-614.

19. Kim, G.M., S. Kawai, M. Nagashio, H. Kawakatsu, and J. Brugger
Nanomechanical structures with 91 MHz resonance frequency fabricated by local deposition and dry etching
Journal of Vacuum Science & Technology B, 2004. **22**(4): p. 1658-1661.

20. Bucher, V., J. Brugger, D. Kern, G.M. Kim, M. Schubert, and W. Nisch
Electrical properties of light-addressed sub-mu m electrodes fabricated by use of nanostencil-technology
Microelectronic Engineering, 2002. **61-2**: p. 971-980.

21. Vroegindeweij, F., E.A. Speets, J.A.J. Steen, J. Brugger, and D.H.A. Blank
Exploring microstencils for sub-micron patterning using pulsed laser deposition
Applied Physics a-Materials Science & Processing, 2004. **79**(4-6): p. 743-745.

22. Cojocaru, C.V., C. Harnagea, A. Pignolet, and F. Rosei
Nanostenciling of functional materials by room temperature pulsed laser deposition
IEEE Transactions on Nanotechnology, 2006. **5**(5): p. 470-477.

23. Cojocaru, C.V., C. Harnagea, F. Rosei, A. Pignolet, M.A.F. van den Boogaart, and J. Brugger
Complex oxide nanostructures by pulsed laser deposition through nanostencils
Applied Physics Letters, 2005. **86**(18).

24. Fulton, T.A. and G.J. Dolan
Observation of Single-Electron Charging Effects in Small Tunnel-Junctions
Physical Review Letters, 1987. **59**(1): p. 109-112.

25. Schallenberg, T., C. Schumacher, and W. Faschinger
In situ structuring during MBE regrowth with shadow masks
Physica E-Low-Dimensional Systems & Nanostructures, 2002. **13**(2-4): p. 1212-1215.

26. Tsang, W.T. and M. Ilegems
Selective Area Growth of Gaas/Alxga1-Xas Multilayer Structures with Molecular-Beam Epitaxy Using Si Shadow Masks
Applied Physics Letters, 1977. **31**(4): p. 301-304.

27. Deshmukh, M.M., D.C. Ralph, M. Thomas, and J. Silcox
Nanofabrication using a stencil mask
Applied Physics Letters, 1999. **75**(11): p. 1631-1633.

28. Kohler, J., M. Albrecht, C.R. Musil, and E. Bucher
Direct growth of nanostructures by deposition through an Si3N4 shadow mask
Physica E, 1999. **4**(3): p. 196-200.

29. Ono, K., H. Shimada, S.I. Kobayashi, and Y. Ootuka
A new fabrication method for ultra small tunnel junctions
Japanese Journal of Applied Physics Part 1-Regular Papers Short Notes & Review Papers, 1996. **35**(4A): p. 2369-2371.

30. Burger, G.J., E.J.T. Smulders, J.W. Berenschot, T.S.J. Lammerink, J.H.J. Fluitman, and S. Imai
High-resolution shadow-mask patterning in deep holes and its application to an electrical wafer feed-through
Sensors and Actuators a-Physical, 1996. **54**(1-3): p. 669-673.

31. Arcamone, J., A. Sanchez-Amores, J. Montserrat, M.A.F. van den Boogaart, J. Brugger, and F. Perez-Murano
Dry etching for the correction of gap-induced blurring and improved pattern resolution in nanostencil lithography
Journal of Micro/Nanolithography, MEMS and MOEMS, 2007. **6**(1): p. 013005-7.

32. van den Boogaart, M.A.F., L.M. Doeswijk, and J. Brugger
Silicon-supported membranes for improved large-area and high-density micro/nanostencil lithography
IEEE Journal of Microelectromechanical Systems, 2006. **15**(6): p. 1663-1670.

33. van den Boogaart, M.A.F., M. Lishchynska, L.M. Doeswijk, J.C. Greer, and J. Brugger
Corrugated membranes for improved pattern definition with micro/nanostencil lithography
Sensors and Actuators a-Physical, 2006. **130**: p. 568-574.

34. Rius, G.
Fabrication of NEMS structures by EBL
Master thesis, UAB (2005)

35. Campabadal, F., S. Ghatnekar-Nilsson, G. Rius, C. Fleta, J. Rafi, E. Figueras, and J. Esteve
CMOS degradation effects due to electron beam lithography in smart NEMS fabrication
in the proceedings of the *SPIE*. 2005.

36. Ghatnekar-Nilsson, S., E. Forsen, G. Abadal, J. Verd, F. Campabadal, F. Perez-Murano, J. Esteve, N. Barniol, A. Boisen, and L. Montelius
Resonators with integrated CMOS circuitry for mass sensing applications, fabricated by electron beam lithography
Nanotechnology, 2005. **16**(1): p. 98-102.

37. Forsen, E., S.G. Nilsson, P. Carlberg, G. Abadal, F. Perez-Murano, J. Esteve, J. Montserrat, E. Figueras, F. Campabadal, J. Verd, L. Montelius, N. Barniol, and A. Boisen
Fabrication of cantilever based mass sensors integrated with CMOS using direct write laser lithography on resist
Nanotechnology, 2004. **15**(10): p. S628-S633.

38. Bruce, R.H. and G.P. Malafsky
High-Rate Anisotropic Aluminum Etching
Journal of the Electrochemical Society, 1983. **130**(6): p. 1369-1373.

39. Likharev, K.K.
Nano and Giga Challenges in Microelectronics
Elsevier ed, 2003. 27-68.

CHAPTER 5

EXPERIMENTAL CHARACTERIZATION OF NEMS/CMOS DEVICES

I. Experimental procedure and measurement set-up ... 156
II. CCII circuit characterization ... 158
III. Electrical measurements of the frequency response of integrated resonators ... 159
III.1. Electrical measurement of in-plane vibrating cantilevers ... 159
III.1.a. Samples characteristics ... 159
III.1.b. Experimental results ... 161
III.1.b.i) Measurements in air with set-up 1 ... 161
III.1.b.ii) Measurements in vacuum with set-up 2 ... 162
III.1.b.iii) Estimation of the Young modulus of the structural layer ... 163
III.1.b.iv) Electrical results summary ... 164
III.1.c. Analysis of results ... 165
III.1.c.i) Estimation of the fringing field parasitic capacitance C_{PA} ... 165
III.1.c.ii) Driving voltage effect: spring-softening ... 165
III.1.c.iii) Q factor evolution as a function of the pressure ... 167
III.1.c.iv) Estimation of critical deflection ... 168
III.1.c.v) Noise considerations ... 169
III.2. Electrical measurement of out-of-plane vibrating quad-beams ... 171
III.2.a. Samples characteristics ... 171
III.2.b. Experimental results ... 171
III.2.b.i) Measurements in air with set-up 1 ... 172
III.2.b.ii) Measurements in vacuum with set-up 2 ... 172
III.2.b.iii) Electrical Results Summary ... 173
III.2.c. Analysis of results ... 174
III.2.c.i) Estimation of the fringing field parasitic capacitance C_{PA} ... 174
III.2.c.ii) Q factor evolution as a function of the pressure ... 174
III.2.c.iii) Driving voltage effects ... 175
Conclusion of chapter 5 ... 177
Bibliographical references ... 178

The scope of this chapter is the electrical characterization of our NEMS/CMOS system. The samples have been fabricated following technological processes described in chapter 4. The experimental set-up as well as the CCII circuit characterization will be briefly described.

This chapter is emphasized on electrical measurements of frequency spectra of two types of integrated resonators: in-plane vibrating cantilevers and out-of-plane vibrating quad-beams (QB). The main features of their magnitude and phase responses measured in air and in vacuum are analyzed. The accuracy of the RLC model is discussed.

I. Experimental procedure and measurement set-up

We have performed all these measurements at the Electronic Circuit and Systems laboratory from the Escola Tècnica Superior de Enginyeria of Universitat Autònoma de Barcelona. Two different set-ups have been used: a probe station for measurements in air (set-up 1) and a vacuum chamber with electrical feed-through (set- up 2).

The electrical detection set-up comprising the probe station (SÜSS MICROTEC PA 200) is sketched in Figure 1. Its main elements are:

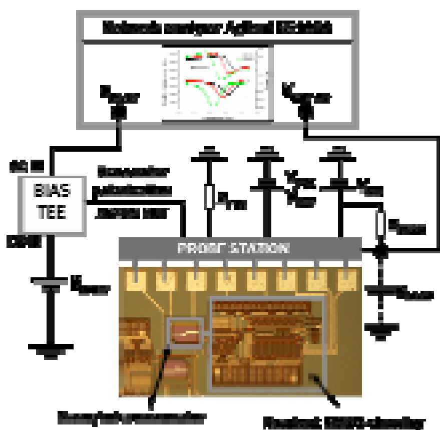

Figure 1. Experimental set-up based on a probe station

- a 16 probes card to access the contact pads
- a bias tee (MINI-CIRCUITS, ZFBT-4R2GW) to sum DC, $V_{IN\ DC}$, and AC, $V_{IN\ AC}$, voltages in order to drive the resonator. $V_{IN\ AC}$ is supplied by a network analyzer
- the network analyzer (AGILENT E5100A) sweeps a programmable frequency range
- the amplified output current of the CMOS circuit is externally converted into a voltage, $V_{OUT\ AC}$, by flowing into the tunable resistor R_{LOAD}
- $V_{OUT\ AC}$ is measured through the network analyzer whose adjustable input impedance is set to 1 MΩ

Samples pre-tested with the probe station can be measured with the second set-up that is adapted to vacuum measurements. This set-up is very similar to the other except that there is no probe station inside the vacuum chamber. Hence, NEMS/CMOS chips are mounted on a printed circuit board (PCB) (Cu lines), and wire bonded to it with Al wires by non-thermal welding based on ultrasounds. SMA connectors placed on the edge of the PCB are cabled to electrical feed-through mounted on the chamber wall. Following this procedure, air and vacuum measurements can be made; nevertheless it must be considered that the wire bonding of the samples requires an additional preparation step with respect to the direct characterization with set-up nº1, and only a limited number (one or two) of devices can be contacted per chip.

Using both set-ups, V_{POL} (see chapter 3) has been set to 2 V (although its optimum value is 1 V) so that the same DC source can simultaneously polarize V_{REF} and V_{POL}. In particular, this solution allowed reducing the number of connectors in the PCB for measurements in vacuum.

MEASUREMENT OF THE FREQUENCY RESPONSE OF A RESONATOR WITH A NETWORK ANALYZER

The network analyzer provides the frequency response in terms of magnitude and phase of the ratio $V_{OUT\,AC}/V_{IN\,AC}$ (also named voltage gain in chapter 3, eq.III-13). A frequency span centered on a given value can be programmed. For any measurement, a trade-off must be found between the number of points of the scan and the narrowness of the band-pass filter applied around each frequency point, otherwise the scan can be very slow.

The magnitude response delivered by the network analyzer is $\Re_{NA}$ given by:

$$\Re_{NA}(dB) = \textit{voltage gain} = 20\log\frac{V_{OUT\,AC}}{V_{IN\,AC}} \tag{V.1}$$

I_{MEMS}, the total AC current originating from the resonator and given by $I_{MEMS} = I_M + I_W + I_{PA}$, can be estimated from $\Re_{NA}$ in the following way:

$$\Re_{NA}(dB) = 20\log\frac{V_{OUT\,AC}}{V_{IN\,AC}} = 20\log\frac{M\,N\,R_{LOAD}I_{MEMS}}{V_{IN\,AC}} \tag{V.2}$$

where $M\,N = 100$ according to the CCII design, what results in:

$$I_{MEMS} = \frac{V_{IN\,AC}}{100\,R_{LOAD}}10^{\frac{\Re_{NA}}{20}} \tag{V.3}$$

To estimate the motional current, the response out of resonance must be simply subtracted to the one in resonance:

$$I_M(f) = \frac{V_{IN\,AC}}{100\,R_{LOAD}}\left(10^{\frac{\Re_{NA_IN\,RESONANCE}}{20}} - 10^{\frac{\Re_{NA_OUT\,RESONANCE}}{20}}\right) \tag{V.4}$$

What we will further name the resonance current I_{RES} corresponds to the maximum motional current, i.e. at the resonance frequency: $I_{RES} = I_M(f_{RES}) = I_{M\,MAX}$.

An additional and very interesting capability of the network analyzer is the calibration of the background signal. As mentioned previously, this specific signal, originating from parasitic capacitances cross-talk, can be so high that the resonance peak is masked. The first step of the calibration procedure consists in measuring the background signal by normally polarizing the CCII and by polarizing the resonator with $V_{IN\,AC} \neq 0$ and $V_{IN\,DC} = 0$ so that the resonator is not excited but its capacitances (parasitic and static) already produce a current. Once the spectrum is recorded, the calibration option is activated and $V_{IN\,DC}$ is applied to the device. In real time, the background signal is subtracted to the newly recorded signal containing the resonance peak: in this way, the resonance peak is highlighted. The response of the network analyzer becomes:

$$\textit{calibrated signal}(dB) = 20\log\frac{V_{OUT\,AC-RES}}{V_{OUT\,AC-BS}} \tag{V.5}$$

where $V_{OUT\,AC\text{-}RES}$ is the output signal with resonance (with $V_{IN\,DC} \neq 0$), i.e. of the $R_M L_M C_M // C_W // C_{PA}$ element, while $V_{OUT\,AC\text{-}BS}$ is the output signal without resonance, i.e. the background signal (with $V_{IN\,DC} = 0$), that corresponds to the $C_W // C_{PA}$ element.

Out of resonance, the magnitude should be 0. In practice, there is a slight offset with respect to 0 that is likely due to a perturbation caused by $V_{IN\ DC}$. Within the calibrated signal spectrum, the most interesting feature is ΔdB, the amplitude of the resonance peak in dB with respect to the offset. At resonance, the value of I_{MEMS} is $I_{MEMS\ MAX}$ which can be calculated in the following way

$$I_{MEMS\ MAX} = I_{MEMS_BS} 10^{\Delta dB/20} \tag{V.6}$$

where I_{MEMS_BS} is the resonator current without the resonance contribution given by eq.(V.3):

$$I_{MEMS_BS} = \frac{V_{IN\ AC}}{100\, R_{LOAD}} 10^{\frac{\Re_{NA}}{20}} \tag{V.7}$$

here, $\Re_{NA}$ is the network analyzer response without nor calibration neither resonance. Computing eq. (V.6) and (V.7), $I_{MEMS\ MAX}$ at resonance is finally obtained:

$$I_{MEMS\ MAX} = \frac{V_{IN\ AC}}{100\, R_{LOAD}} 10^{\frac{\Delta dB + \Re_{NA}}{20}} \tag{V.8}$$

and

$$I_{RES} = \frac{V_{IN\ AC}}{100\, R_{LOAD}} \left(10^{\frac{\Delta dB + \Re_{NA}}{20}} - 10^{\frac{\Re_{NA}}{20}} \right) \tag{V.9}$$

COMMENT ON SATURATION ISSUES:

In chapter 3, the condition of saturation of the output voltage was defined through eq.(III.11). Thus, it is possible to define the saturation threshold in the response of the network analyzer. Computing eq.(V.2) and (III.11), the maximum allowed response to avoid saturation is:

$$\Re_{NA\ \ MAX-SAT}(dB) = 20 \log \frac{100\, R_{LOAD}}{V_{IN\ AC}} \frac{V_{R_{POL}}}{R_{POL}} = 20 \log \frac{100\, R_{LOAD}}{V_{IN\ AC}} I_{BIAS} \tag{V.10}$$

As it depends on well-known experimental parameters, this calculation is straightforward. Then, if during the measurements $\Re_{NA}$ is smaller than this criteria, then one can be sure that the system is not operated in its saturation mode.

II. CCII circuit characterization

The experimental response of the CCII circuit has been directly measured on a CCII containing an integration area. A serial resistor of value R_{IN} is inserted between the AC supply of the network analyzer and the bias tee. The resulting test current is approximately given by

$$I_{TEST} \approx \frac{V_{IN\ AC}}{R_{IN}} \tag{V.11}$$

To extract the corresponding transimpedance gain from $\Re_{NA}$, eq.(V.1) is computed with eq.(V.11):

$$20\log\frac{V_{OUT\,AC}}{I_{TEST}} = G_{TRANSIMPEDANCE} = 20\log R_{IN} + \Re_{NA} \quad \text{(V.12)}$$

For the experimental determination of the Bode diagram, a relatively high value for R_{LOAD} is chosen: in this way, the bandwidth is limited by the output R_{LOAD} // C_{LOAD} low-pass filter and not by the internal high impedance pole. Thus, the parasitic load C_{LOAD} capacitance can be estimated from the cut-off frequency (-3 dB) according to eq.III.7. The experimental spectrum of the transimpedance gain is shown in Figure 2:

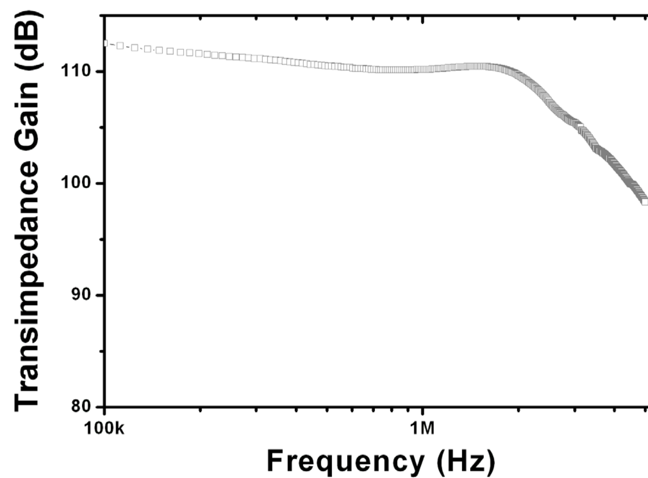

Figure 2. Experimental Bode diagram of the CCII circuit with R_{LOAD} = 2500 Ω and R_{IN} =1 MΩ

The response is not perfectly flat but the gain plateau is around 110 dB. This value is in good concordance with the theoretical value of 108 dB given by $20\log(100\,R_{LOAD})$. An approximate value of 30 pF for C_{LOAD} is extracted from the cut-off frequency.

III. Electrical measurements of the frequency response of integrated resonators

Electrical measurements of resonance spectra of integrated cantilevers and QB are the topic of this section. Interesting features and signal level of the measured responses are discussed.

III.1. Electrical measurement of in-plane vibrating cantilevers

III.1.a. Samples characteristics

The cantilever beams are made of polysilicon and have been defined either by electron-beam (eBL) or by nanostencil lithography (nSL). As detailed in chapter 4, the fabrication process based on nSL provided a large amount of devices, about 500 in total. However, to be able to

introduce some changes in the design of the devices, some new prototypes have punctually been fabricated by eBL.

The devices are either single or double cantilevers (orthogonally oriented one to each other) operated in the fundamental in-plane flexural mode. Individually, single and each beam of the double cantilevers exhibit the same electrical behavior. However, double beams features some interesting properties regarding mass sensing and also in terms of electrical response if they can be successfully coupled. These aspects will be tackled in detail in chapter 6. Single and double cantilevers are depicted in Figure 3:

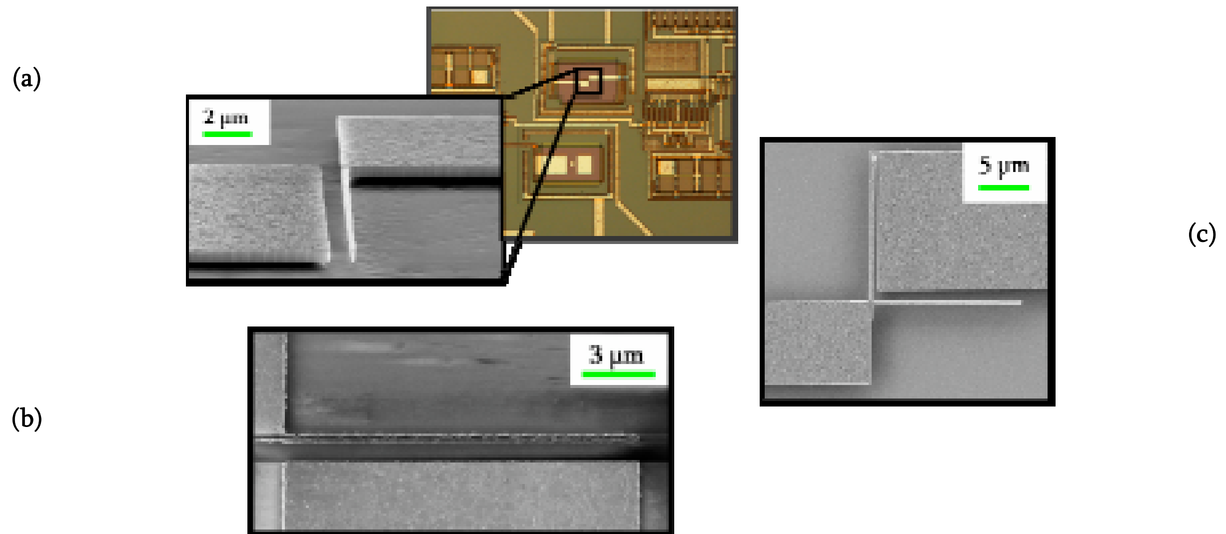

Figure 3. Images of fully fabricated CMOS integrated cantilevers. (a) Optical image of the CCII circuit and of the juxtaposed cantilever zoomed in the inset (tilted SEM image); (b) SEM image of a single cantilever whose edges are rough due to a defect in the patterning; (c) SEM image of a double cantilever

The geometrical dimensions measured by SEM of five characteristic cantilevers are reported in Table V - 1. The lithography technique employed for their patterning is specified. l is the cantilever length, b the width, h the thickness[1] and d the cantilever-driver gap.

Reference	Simplified Denomination	l (µm)	b (nm)	h (nm)	d (nm)	Lithography technique
3157-11-B5-c10	A	14.45	285	560	790	nSL
3157-13-c3 CD3	B	14.5	400	460	600	eBL
3157-13-c3 CD4	C	14.6	400	460	400	eBL
3157-13-c3 CD6	D	14.3	400	460	400	eBL
3157-11-F1 c3	E	14.5	260	570	820	nSL

Table V - 1. Cantilever samples characteristics. Geometrical dimensions measured by SEM

[1] some deviations are observable concerning the thickness of the devices. This difference is attributed to the fact that these samples come from different wafers that underwent process fluctuations. Actually, samples A and E are of the same wafer and $h \approx 560$ nm, while B, C and D are from another wafer and $h \approx 460$ nm.

III.1.b. Experimental results

The correct operation of in-plane vibrating cantilevers has been demonstrated in air and in vacuum: the capacitive detection scheme including the CCII CMOS circuit successfully transduced mechanical oscillations into an electrical signal so that the mechanical frequency response, including the resonance peak, could be electrically detected. The obtained quality factors are around 15 in air, while they reach about 9700 in vacuum (at 4.10^{-3} mBar). This is a very high value despite the fact that polysilicon is a relatively disordered structural material.

III.1.b.i) Measurements in air with set-up 1

Figure 4 depicts characteristic responses of cantilevers (A and D) operated in air. In these measurements, the background signal has been pre-calibrated according to the aforementioned procedure. The resonance frequency of these cantilevers can be tuned by varying the applied DC voltage and a clear spring-softening effect is seen with increasing $V_{IN\ DC}$. The main structural difference between cantilevers A and D is the transducing gap: 800 and 400 nm respectively. This logically results in a better electrostatic coupling for D illustrated by a higher magnitude and a greater phase change: to reach a magnitude of 1 dB, A and D need 23 and 8 V respectively, corresponding to 17 and 20 ° of phase change. It is clear that future designs of low power NEMS/CMOS systems require taking advantage of the nanopatterning techniques to define narrow gaps in the deep submicron range.

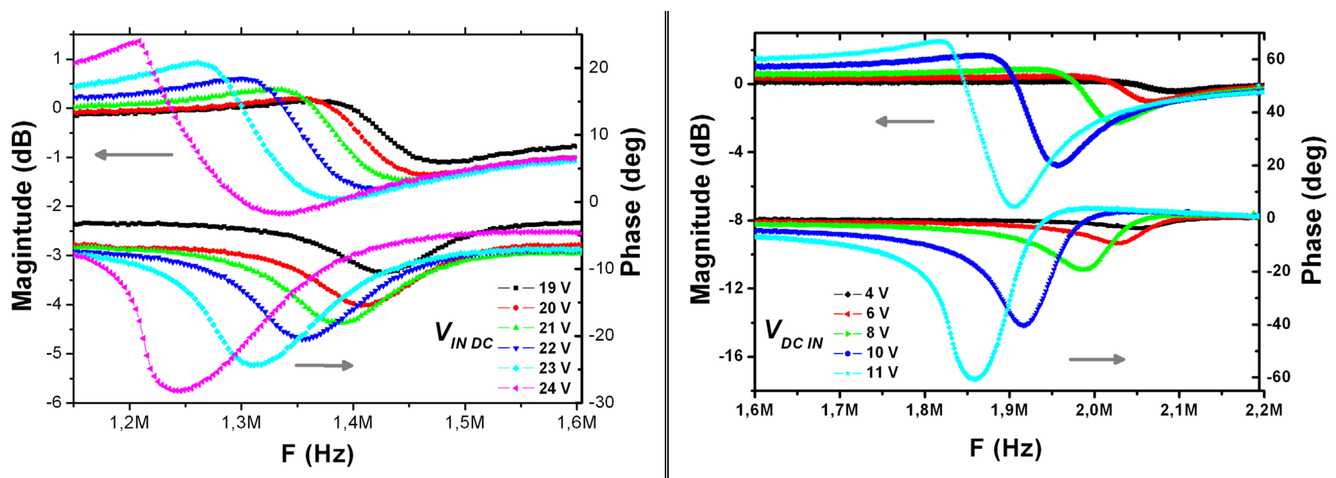

Figure 4. Calibrated resonance spectra in air of cantilever A (left) and D (right) for several $V_{IN\ DC}$ voltages. $V_{IN\ AC}$ is respectively 2.8 and 0.9 V peak-peak (pp) for A and D

Furthermore, after a certain threshold of $V_{IN\ DC}$, a very interesting nonlinear behavior is observable both cantilevers of Figure 4 and Figure 5. This means that the critical oscillation amplitude (see chapter 2) has been exceeded what leads to hysteretic frequency spectra that could provide novel applications like memory elements based on NEMS [1].

In this sense, the spectrum of Figure 5, recorded at $V_{IN\ DC}$ =20 V (non pre-calibrated curve), starts to exhibit a nonlinear behavior whereby the resonance peak takes the form of a spike and its related phase change is about to get an infinite vertical slope. Regarding the final objective of implementing nanoresonators as mass sensors, it is clear that being able to reach the nonlinear behavior of the cantilever with a low enough $V_{IN\ DC}$ voltage (so that it remains inferior to the pull-

in voltage threshold) is a clear advantage in terms of mass sensitivity. Indeed, it is assumed [2] that the sensitivity is the highest at the onset of nonlinearity (because of the infinite slope).

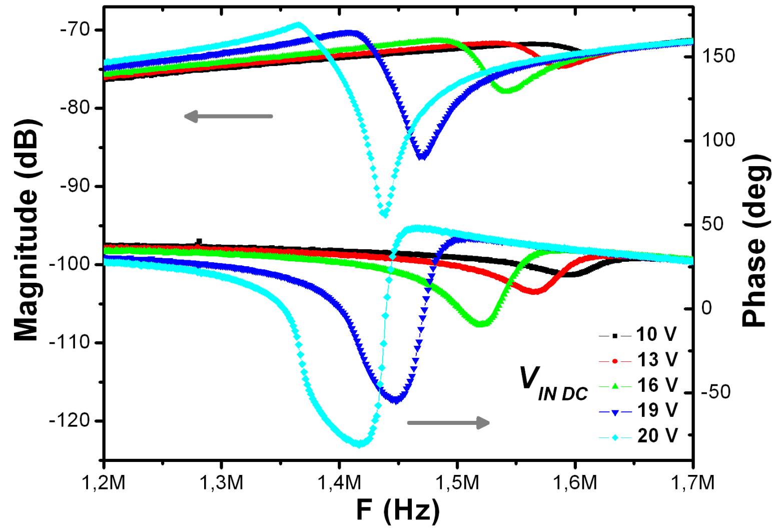

Figure 5. Non-calibrated resonance spectra in air of cantilever B for $V_{IN\ AC}$=0.9 Vpp and several $V_{IN\ DC}$

III.1.b.ii) Measurements in vacuum with set-up 2

The chip containing cantilever E has been wire bonded and it has been measured in the vacuum chamber of set-up 2 whose minimum pressure is limited to about 10^{-3} mBar.

Figure 6 depicts two spectra measured at P=10^{-2} mBar. Interestingly, very low driving voltages are enough for polarizing the device: 1 or 2 V DC (1 V is enough actually) added to a 0.092 V AC. A 2 V DC polarization is sufficient to provoke a strong nonlinear behavior yielding almost vertical slopes both in magnitude and in phase. A 130 ° phase change is obtained, not very far from the ideal case of 180 °. The Q factors are respectively 9150 and 6650 for 1 and 2 V ($V_{IN\ DC}$) while they are between 10 and 20 in air. This great enhancement is due to the lower level of pressure what drastically reduces the viscous damping.

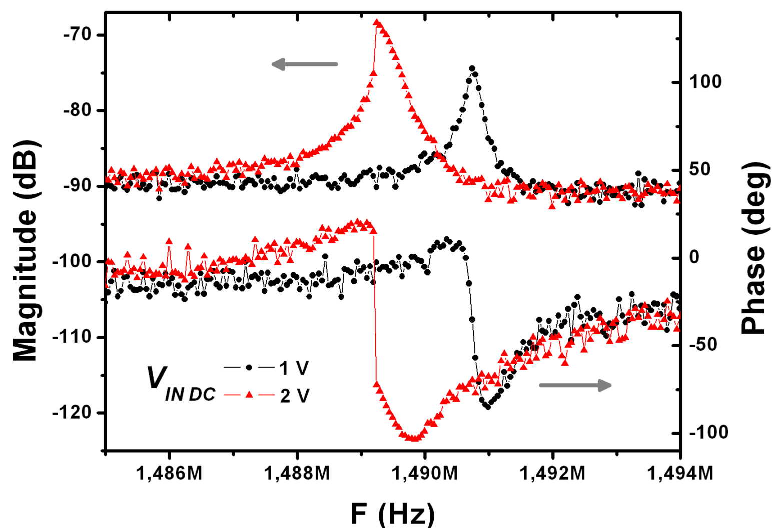

Figure 6. Non-calibrated resonance spectra in vacuum of cantilever E measured at P=10^{-2} mBar for $V_{IN\ DC}$=1 and 2 V and $V_{IN\ AC}$=92 mV pp.

It has to be noticed that these spectra feature a strange shape in the sense that the magnitude almost does not exhibit any anti-resonance peak. To understand this phenomenon, an electrical simulation (see chapter 3, section II.2.c.i) based on experimental parameters is performed and depicted in Figure 7:

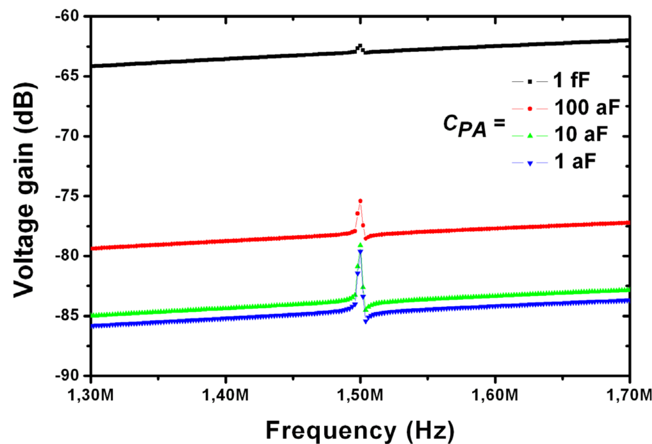

Figure 7. HSPICE simulation of cantilever E. All variable parameters are calculated basing on real geometrical dimensions and on the measured Q factor (=9150) for $V_{IN\ DC}$=1 V, C_{PA2}=50 fF, C_{DC}≈C_O=89 aF

The information provided by the simulation is coherent with the quasi-absence of anti-peak in the experimental curve (in fact, in Figure 6 it seems that there is a small anti-peak but it can not be well visualized because of the too narrow frequency span compared to Figure 7). In fact, the quasi-absence of anti-peak can only be explained if C_{PA} is very low.

According to the simulation, a background signal of -90 dB (see figure Figure 6) results from values of C_{PA} below 10 aF, e.g. much smaller than C_{DC} (normally, C_{PA} is in the order of C_{DC}). Consequently, the absence of anti-peak seems to be related to a reduced C_{PA} but there is no apparent reason to explain this phenomenon.

III.1.b.iii) Estimation of the Young modulus of the structural layer

Statistics on experimental and theoretical resonance frequency have been done. For samples fabricated by nSL, a very good matching is achieved setting a Young modulus of 130 GPa for the structural polysilicon layer. For samples defined by eBL, a non-explained slight distortion is found between theory and experiment. This may be attributed to the fact that these samples underwent a longer wet etch to release the structures what also partially released their anchor. This probably makes the ensemble less stiff and thereby they resonate at a lower frequency. These results are summarized in Table V - 2:

Cantilever	f_{TH} (MHz)	[1]f_{EXP} (MHz)
A	1.65	1.63
E	1.49	1.49
B	2.3	1.93
C	2.26	1.86
D	2.36	2.15

Table V - 2. Theoretical resonance frequency calculated with E=130 GPa compared to the experimental value.

[1] the experimental resonance frequency is extrapolated at $V_{IN\ DC}$=0 from a linear fit of spring-softening curve

III.1.b.iv) Electrical results summary

The electrical results of cantilevers A, B, C, D and E are summarized in Table V - 3 and Table V - 4. The pull-in voltage V_{PI} (see chapter 2) is calculated with a spring constant of α_2 =2/3.

Table V - 3 reports data with calibrated measurements. $\Re$(dB) means the background signal level and ΔG(dB) the relative amplitude of the resonance peak of the calibrated signal. I_{RES_EXP} is calculated according to eq.(V.9) and I_{RES_TH} is calculated as $V_{IN\ AC}/R_M$ (see chapter 2) where R_M is the theoretical motional resistance.

Cant.	R_{LOAD} R_{POL}	V_{PI} (V)	$V_{IN\ DC}$ (V)	$V_{IN\ AC}$ (V_{PP})	Q	$\Re$(dB) BS	ΔG(dB)	I_{RES_EXP} (nA)	I_{RES_TH} (nA)
A	800Ω	28	19	2.8	15	-60	0.26	1	5
	180kΩ		23		20		1,03	4,4	8
C	800Ω 184kΩ	48	8	0.9	14	-66	0.75	0.5	1.7
			10		15		1.43	1	2.9
			11		18.5		2.06	1.5	4.2
D	800Ω	49	10	0.9	13	-68	1.69	1	2.4
	184kΩ		11		17		2.51	1.5	3.7

Table V - 3. Electrical measurements results obtained with background signal calibration.

Table V - 4 reports data without background signal calibration. G(dB)BS means the background signal level and G(dB)Res the amplitude of the resonance peak. I_{RES_XP} and I_{RES_TH} are obtained following the method exposed for Table V - 3.

Cant.	R_{LOAD} R_{POL}	V_{PI} (V)	$V_{IN\ AC}$ (mV pp)	$V_{IN\ DC}$ (V)	Q	P (mBar)	G(dB) BS	G(dB) Res	I_{RES_EXP} (nA)	I_{RES_TH} (nA)
E	700Ω	25	92	1	9150	10^{-2}	-89.5	-74.4	0.21	0.29
	180kΩ			2	6650			-68.4	0.46	0.86
E	700Ω 180kΩ	25	92	1	9650	4.10^{-3}	-90	-75.75	0.17	0.31
					9150	10^{-2}		-76	0.17	0.29
					7640	10^{-1}		-77.2	0.14	0.25
					3880	0.9		-83.44	0.05	0.12
B	800Ω 184kΩ	48	900	16	8	1000	-73.3	-71.34	0.6	0.8
				19	10		-74.1	-70.25	1.24	1.35
				21	15		-75.3	-68.9	2.1	2.5

Table V - 4. Electrical measurements results obtained without background signal calibration.

The first statement to do is the accuracy of the pull-in voltage calculated with α_2=2/3. It has been observed a good correspondence between the theoretical value and the experimental value of pull-in.

Concerning the RLC model accuracy for cantilevers, the experimental value of I_{RES_EXP} is systematically smaller than I_{RES_TH} by a factor two or three. Taking into account all the measurement uncertainties regarding the geometrical dimensions and the Q factor whose precise estimation is difficult (I_{RES_TH} is directly linked to Q, as Q determines R_M through eq.III.15), this model can be considered relatively precise. It is more qualitative than quantitative, however to roughly predict the order of magnitude of the resonance signal, it constitutes an interesting tool.

This model is valid only in the mechanical linear regime of the cantilever. Since the model relies on a constant stiffness, its precision degrades when nonlinear resonance behavior appears.

III.1.c. Analysis of results

Different features of the experimental behavior of cantilevers are analyzed in this section.

III.1.c.i) Estimation of the fringing field parasitic capacitance C_{PA}

In order to estimate C_{PA}, a comparison is carried out between experimental curves and simulated resonance spectra obtained with real parameters. The simulation value of C_{PA} is obtained by fitting the level of background signal.

We mainly attribute the parallel parasitic capacitance C_{PA} to the existence of a fringing electrostatic field in the cantilever/driver 'lateral' (in-plane) capacitor. This extra-field cannot be neglected since gap and height of the capacitor plates are of comparable dimensions (the height is not infinite unlike in the ideal parallel-plates approximation). In our case, gap (d) and thickness (h) are effectively comparable. Thereby, the theoretical expression of the total capacitance can be approximated as:

$$C_{TOT} \approx C_{DC}\left[1+\frac{2d}{\pi h}\ln\frac{\pi h}{d}+\frac{2d}{\pi h}\ln\left(1+\frac{2b}{d}+2\sqrt{\frac{b}{d}+\frac{b^2}{d^2}}\right)\right]=C_{DC}+C_{PA} \tag{V.13}$$

hence,

$$C_{PA} \approx C_{DC}\left[\frac{2d}{\pi h}\ln\frac{\pi h}{d}+\frac{2d}{\pi h}\ln\left(1+\frac{2b}{d}+2\sqrt{\frac{b}{d}+\frac{b^2}{d^2}}\right)\right] \tag{V.14}$$

These results are reported in Table V - 5: C_{PA} is compared to the (theoretical) static capacitance C_{DC} for a given $V_{IN\ DC}$ voltage:

Cantilever	$V_{IN\ DC}$ (V)	C_{DC_TH} (fF)	C_{PA_SIMUL} (fF)	C_{PA_TH} (fF)
B	16	0.10	0.175	0.20
D	10	0.15	0.275	0.25

Table V - 5. Estimations of C_{PA} comparing experimental data (fitted with simulations) and analytical results

There is a good concordance between experimental results (fitted to simulation data) and analytical values: for this reason, the magnitude of C_{PA} can be mainly attributed to the fringing field.

III.1.c.ii) Driving voltage effect: spring-softening

As mentioned in chapter 2, the driving voltage ($V_{IN\ AC}$ + $V_{IN\ DC}$) has an incidence on the resonance frequency value and may tune it up or down. In all these experiments, a decrease of the resonance frequency with increasing driving voltage has been observed what corresponds to the so-called spring-softening effect. This means that for cantilevers, the electrostatic behavior dominates over mechanical stiffening (see chapter 2, section II.3.c).

In practice, the resonance frequency can be tuned down by varying only the applied DC voltage (assuming $V_{IN\ DC} >> V_{IN\ AC}$): in this case, it linearly decreases as a function of $V_{IN\ DC}^2$ (eq. II-81). In Figure 8, a typical spring-softening curve obtained with cantilever A is shown:

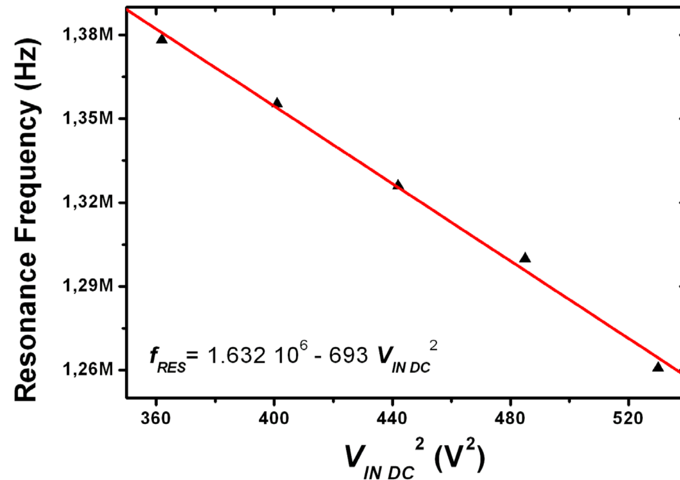

Figure 8. Resonance frequency dependence upon $V_{IN\ DC}$ of cantilever A
The linear fit is plotted in red and the fitted linear equation is indicated

K, defined as the electromechanical coupling factor, can be extracted from experimental curves by putting the equation of the linear fit under the form $f_{RES} = f_0\left(1 - K V_{IN\ DC}^2\right)$ (eq.II-81), where f_0 is the natural resonance frequency.

K can be expressed theoretically as a function of material and geometrical parameters eq.(II-81):

$$K = \frac{3\varepsilon_0 l^4}{4E b^3 d^3} \tag{V.15}$$

The results of the comparison between theory and experiment are reported in Table V - 6:

Cant.	K_{TH}	K_{EXP}
A	1.9 10^{-4}	4.2 10^{-4}
B	2 10^{-4}	4.3 10^{-4}
C	5 10^{-4}	9 10^{-4}
D	6 10^{-4}	9 10^{-4}
E	2.3 10^{-4}	3.3 10^{-4}

Table V - 6. Comparison of theoretical and experimental electromechanical coupling factors

The experimental value is systematically higher than the theoretical one. This can be partially explained by the fact that the gap is overestimated in eq.(V.15) as it is considered in a non-polarized configuration. When the cantilever is polarized with $V_{IN\ DC}$, the cantilever bends towards its driving electrode and therefore the gap is reduced what contributes to increase *K*.

CANTILEVER BEHAVIOR AT HIGH DRIVING LEVELS

In continuity with chapter 2, the calculation of the transfer function of two parallel branches $R_M L_M C_M // C_{PA}$ leads to two peaks in the amplitude-frequency domain:

- the proper resonance peak whose frequency is given by $f_{RES} = \frac{1}{2\pi\sqrt{L_M C_M}}$
- the so-called anti-resonance peak whose frequency is given by $f_{A-RES} = \frac{1}{2\pi\sqrt{L_M C}}$

with $C = \dfrac{C_{PA} C_M}{C_{PA} + C_M}$

If $C_{PA} >> C_M$, $C \approx C_M$ i.e. f_{RES} is very close to $f_{A\text{-}RES}$ and the anti-peak tends to cancel the resonance peak. If C_M becomes comparable to C_{PA}, then C is no more approximately equal to C_M and the anti-resonance peak gets farther from the resonance frequency towards higher frequencies. In terms of phase, this improvement materializes in the shape of the peak: it takes a 'U-shape' with flat bottom between f_{RES} and $f_{A\text{-}RES}$.

In Figure 9, cantilever B is driven in air at two relatively high DC voltages. Both resonance spectra exhibit very interesting behaviors combining two features: high phase changes and high nonlinearity due to the high driving level.

The observation of the curve recorded at 20 V is consistent with the aforementioned case whereby C_M gets closer to C_{PA}: the phase change is no more a spiky peak but U-shaped. Additionally, a nonlinear behavior starts to appear.

The observation of the curve recorded at 21 V is the continuation of the 20 V curve. f_{RES} and $f_{A\text{-}RES}$ are far from each other (100 kHz) and the nonlinear behavior is much more pronounced: both phase changes are vertical and very important (100 and 180° for f_{RES} and $f_{A\text{-}RES}$ respectively). The phase change related to the anti-peak gets downward by 180°: the analytical calculation of the transfer function always predicts that it should get upwards. This phase decrease is probably a measurement artifact of the network analyzer.

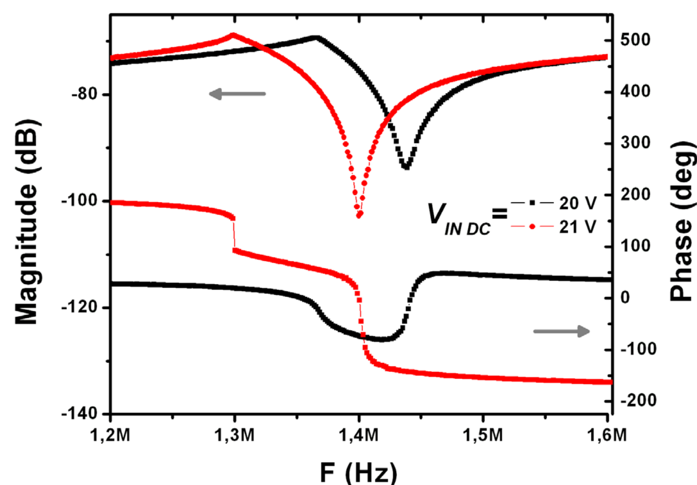

Figure 9. Strongly nonlinear behavior of cantilever B in air (non-calibrated signal). Resonance spectra for $V_{IN\ DC}$=20 and 21 V. $V_{IN\ AC}$=0.9 V pp.

III.1.c.iii) Q factor evolution as a function of the pressure

In Figure 10 and Figure 11, the Q factor is extracted from resonance spectra measured at different levels of pressure and maintaining constant all the other parameters. These graphs must help in further assessing the sources of dissipation affecting the resonator.

Between other interests, information on the Q factor is also important to know if portative vacuum sealed systems are aimed to be developed (the complexity of the packaging would depend much on the required vacuum level).

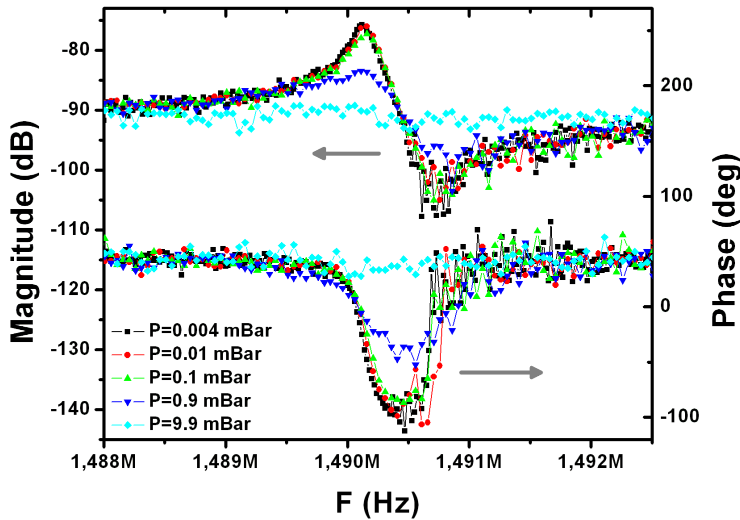

Figure 10. Resonance spectra in vacuum of cantilever E for $V_{IN\,DC}$ =1 V and $V_{IN\,AC}$=92 mV pp
Spectra recorded at several pressures (non-calibrated signal)

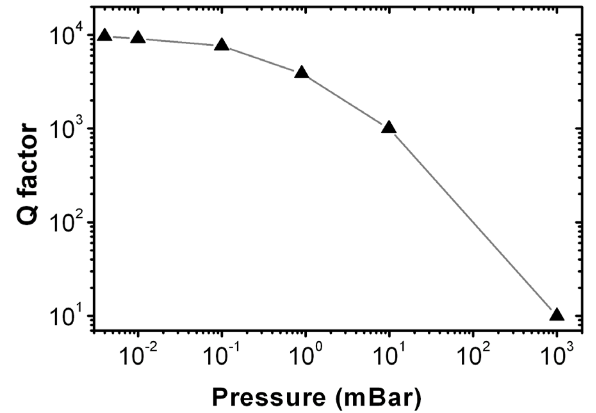

Figure 11. Based on data of Figure 10, the Q factor is plotted as a function of the chamber pressure

From Figure 11, it seems that the most pronounced evolution occurs between 1 Bar and 0.1 mBar: in this range, the Q factor can be enhanced by three orders of magnitude. Below 0.1 mBar the improvement saturates what is in agreement with reported experiments [3, 4]. These results confirm that viscous damping plays a key role regarding the value of the quality factor of nano/ microresonators whereas at low pressure intrinsic mechanisms dominate.

These curves seem quite noisy but this is only due to the remarkably low DC driving voltage (1 V): this makes that the signal magnitude is low (according to eq.III-14 and -15, the motional resistance R_M effectively depends on $V_{IN\,DC}$ and the higher $V_{IN\,DC}$, the lower R_M). Thereby, the signal-to-noise ratio is lowered.

III.1.c.iv) Estimation of critical deflection

It is well-known that a mechanical nonlinear behavior appears in the oscillations of a resonator when its deflection (static or dynamic) exceeds a certain value, named critical amplitude (or deflection) (of which the calculation was detailed in chapter 2). In this section, we propose to study the correlation between the apparition of nonlinear oscillations (visible in almost all the previous experimental curves) and the level of driving voltage. Indeed, the force that mechanically deflects the cantilever is precisely the electrostatic force generated by the driving voltage.

In Table V - 7, the critical deflection x_C is calculated for the samples B and E as a function of characteristic Q-factors: for B (in air), Q between 10 and 100 like in Figure 5 and for E (in vacuum), Q between 1000 and 10000 like in Figure 6. The calculation is based on eq.II-78 for β=1.58 and υ=0.22 [5].

In Table V - 8, the theoretical displacement x of the cantilever tip is calculated for samples B and E as a function of characteristic driving DC voltages (we neglect the time-varying part of the displacement since it is about two orders of magnitude smaller according to our estimations). The calculation is based on eq.II-75 (the spring constant is considered with α_2=0.25 as the displacement is considered in one single point at the cantilever extremity).

Cant.	b (nm)	Q	x_C (nm)
B	400	10	146
		100	46
E	260	1000	9
		10000	3

Table V - 7. Theoretical critical amplitude as a function of the Q-factor. b is the cantilever width

Cant.	Conditions	$V_{IN\ DC}$	x (nm)
B	air	10	29
		15	78
		20	192
E	vacuum	1	0.5
		2	2

Table V - 8. Theoretical deflection of the cantilever extremity for samples B and E as a function of $V_{IN\ DC}$

The Q-factor of cantilever B is around 10 (see Table V - 4) what results in a critical amplitude of 146 nm according to Table V - 7. It is clear from Figure 5 that the nonlinear behavior of B starts at 20 V whose equivalent calculated deflection is 192 nm: both values are in quite good concordance. The same happens with cantilever E whose Q factor and critical amplitude are about 10 000 and 3 nm respectively according to Table V - 4 and Table V - 7. The calculated deflection for 2 V, whereby a strong nonlinear behavior is already visible (see Figure 6), is 2 nm in good concordance with the calculated x_C value (about 3 nm).

These results confirm that a sufficiently high voltage can result in a high enough static deflection so that the cantilever bends too much and comes out of its linear regime (it exceeds x_C).

III.1.c.v) Noise considerations

In this section, theoretically calculated noise levels are compared to experimental signal levels. Mainly three categories of noise may affect the electrical output response: (i) the noise generated by the nanomechanical device, (ii) the one generated by the CMOS circuitry, and (iii) an (external) noise related to the measurement set-up.

First, let us estimate the magnitude of the intrinsic noise of the nanoresonator: we make the assumption that it is exclusively of thermomechanical origin (see chapter 1). Following this approach, the current noise arising from thermomechanical motion [6] is estimated hereafter. According to the equipartition theorem, the thermal energy in the cantilever generates a motion of the cantilever:

$$\frac{1}{2}k_B T = \frac{1}{2} m_{EFF}\, \omega_0^2 \left\langle x_{TH}^2 \right\rangle \tag{V.16}$$

where k_B is the Boltzmann constant, T the temperature, m_{EFF} the efficient mass of the resonator, ω_0 the angular resonance frequency and $\left\langle x_{TH}^2 \right\rangle$ the mean-square resulting displacement of the end of the cantilever.

To simplify the calculation of this term, we consider that the density of displacement noise $\widetilde{x^2(\omega)}$ is constant over the resonator bandwidth (ω_0/Q). In this way, we calculate the effective noise displacement $x_{TH\ N}$ over the considered measurement bandwidth B:

$$\left\langle x_{TH}^2 \right\rangle = \int_0^\infty \frac{\widetilde{x^2(\omega)}}{B} d\omega \approx \int_{\omega_0-\frac{\omega_0}{2Q}}^{\omega_0+\frac{\omega_0}{2Q}} \frac{\widetilde{x^2(\omega)}}{B} d\omega \approx x_{TH\ N}^2 \frac{\omega_0}{BQ} \tag{V.17}$$

Computing now eq.(V.16) with eq.(V.17), the oscillation amplitude due to thermomechanical noise is estimated as:

$$x_{TH\,N} \approx \sqrt{\frac{k_B\, T\, Q\, B}{m_{EFF}\; \omega_0^3}} \tag{V.18}$$

then, computing eq.(V.18) with eq.(II.68), the resulting current noise of these oscillations is:

$$i_{NOISE} \approx \eta\, \omega_0 \left\langle x_{TH} \right\rangle = \frac{\varepsilon\, A}{d^2} V_{IN\,DC} \sqrt{\frac{k_B\, T\, Q\, B}{m_{EFF}\; \omega_0}} \tag{V.19}$$

Calculating this noise for several samples measured either in air or vacuum with a measurement bandwidth B=10 Hz (corresponding to the band-pass filter of the network analyzer), we find that i_{NOISE} is systematically in the order of 10-20 fA RMS.

Let us compare now this value with the equivalent noise current at CCII circuit input (ENCCI). The density of this noise, called D_{ENCCI}, can be calculated dividing the density of the output voltage noise D_{OVN} (obtained by simulation and reported in table III-8) by the transimpedance gain:

$$D_{ENCCI} = \frac{D_{OVN}}{100\, R_{LOAD}} \tag{V.20}$$

For R_{POL}=200 kΩ (see table III-8), D_{ENCCI} ≈0.7 $pA/\sqrt{Hz}$ (RMS). Let us numerically estimate the noise levels for two characteristic samples (cantilevers B and E). The resonator bandwidth BW is calculated according to eq.III-12, then the equivalent noise current at circuit input (ENCCI) is evaluated. From this value, the resonance signal to noise ratio (SNR) is calculated considering the data of Table V - 4. Then, the equivalent voltage gain (see eq.III.13) is calculated:

$$\textit{voltage gain} = 20 \log\left(\frac{ENCCI * 100 * R_{LOAD}}{V_{IN\,AC}} \right) \tag{V.21}$$

As an indication, the background signal level is mentioned as well. The results are reported in Table V - 9.:

Cantilever	Q $V_{IN\,DC}$ (V)	BW (Hz)	ENCCI (A)	SNR (dB)	Voltage gain (dB)	Experimental background signal level (dB)
B	10 (air) 19	140 k	0.26 n	14	-94 for $V_{IN\,AC}$=1 V	-75
E	9150 (vac.) 1	160	9 p	27	-103 for $V_{IN\,AC}$=0.09 V	-90

Table V - 9. Theoretical estimates of the noise generated by the CMOS circuitry based on experimental data

This table reveals that the noise generated by the CMOS circuitry dominates over the thermomechanical noise by at least three orders of magnitude and that the average SNR is around 20 dB. This table also confirms the previous assumption that the background signal results mostly from the parallel stray capacitance C_{PA} and not from the noise level. These data also indicate that the external noise does not seem to play any key role here.

III.2. Electrical measurement of out-of-plane vibrating quad-beams

III.2.a. Samples characteristics

The quad-beams are made of polysilicon and have been defined by electron-beam (eBL) lithography on pre-fabricated CMOS substrates. In this way, it has been possible to create new prototypes in order to optimize the design for an operation in out-of-plane flexion.

Geometrical dimensions measured by SEM of two characteristic QB are reported in Table V - 10. The lithography technique employed for their patterning is specified. L_1 is the plate width, l the beam length, b the beam width, h the thickness and d the QB plate - bottom electrode (substrate) gap.

Reference	Simplified Denomination	L_1 (µm)	l (µm)	b (nm)	h (nm)	d (µm)	Patterning technique	[1]f_{EXP} (MHz)	[2]f_{TH} (MHz)
3157-13-c 19 A6	A	6.25	13.45	765	450	1	eBL	1.50	1.47
3157-13-c 16 A4	B	6	13.3	420	450	1	eBL	1.43	1.17

Table V - 10. QB samples characteristics. Geometrical dimensions measured by SEM

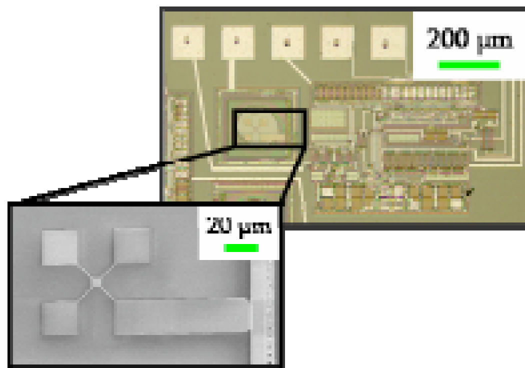

Figure 12. Images of a fully fabricated CMOS integrated quad-beam. Optical image of the CCII circuit and its juxtaposed QB; Inset (SEM image): zoom inside the integration area

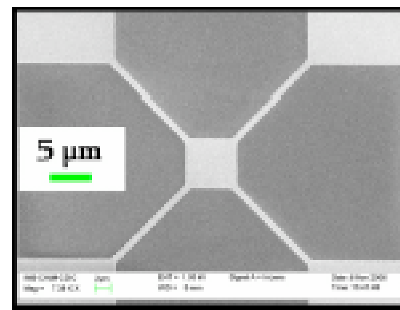

Figure 13. SEM image of a typical QB: central plate and four diagonal beams

III.2.b. Experimental results

The correct operation of out-of-plane vibrating QB has been demonstrated in air and in vacuum: the capacitive detection scheme including the CCII CMOS circuit also successfully transduced mechanical oscillations into an electrical signal so that the mechanical frequency response of the QB, including the resonance peak, could be electrically detected. The obtained quality factors are around 30 in air, while they reach 6500 in vacuum (at 1.1 10^{-2} mBar).

---

[1] the experimental resonance frequency is extrapolated at $V_{IN\,DC}$=0 from a linear fit of spring-softening effect
[2] the theoretical resonance frequency is calculated with method 2 (see chapter 2)

III.2.b.i) Measurements in air with set-up 1

Figure 14 depicts characteristic magnitude and phase responses of a QB (QB B) operated in air. In these measurements, the background signal has been pre-calibrated according to the aforementioned procedure. The resonance frequency can be tuned by varying the applied DC voltage and a clear spring-softening effect is seen in Figure 14 with increasing $V_{IN\,DC}$.

As expected, this QB features much weaker phase and amplitude peaks than cantilevers, first, because of the much higher parasitic feed-through capacitance (related to the anchors), and second, because the transducing gap is as high as high 1 µm. Moreover, it is difficult to reduce this gap as it is determined by the thickness of the sacrificial SiO_2, the CMOS field oxide in this case. At 20 V, typical values of amplitude and phase peaks are 0.03 dB and 0.25° with respect to the background signal, to be compared to typical 1 dB and 30° for an in-plane vibrating cantilever.

Actually, these QB were initially designed to be operated at higher DC driving voltages than the presented 20 V, since they have high pull-in voltages (>50 V) and a big plate area to enhance the capacitive coupling. But an unexpected problem appeared in experimental tests: for voltages superior to 30-35 V the CMOS circuit operation was perturbed. This phenomenon is likely due to the depletion zone that forms at the border of the underlying n-well which serves as driving electrode. This n-well is relatively close to the p-type substrate where n-type transistors are implanted and the extension of the depletion zone probably arrives until the n-type transistors area and perturbs their operation.

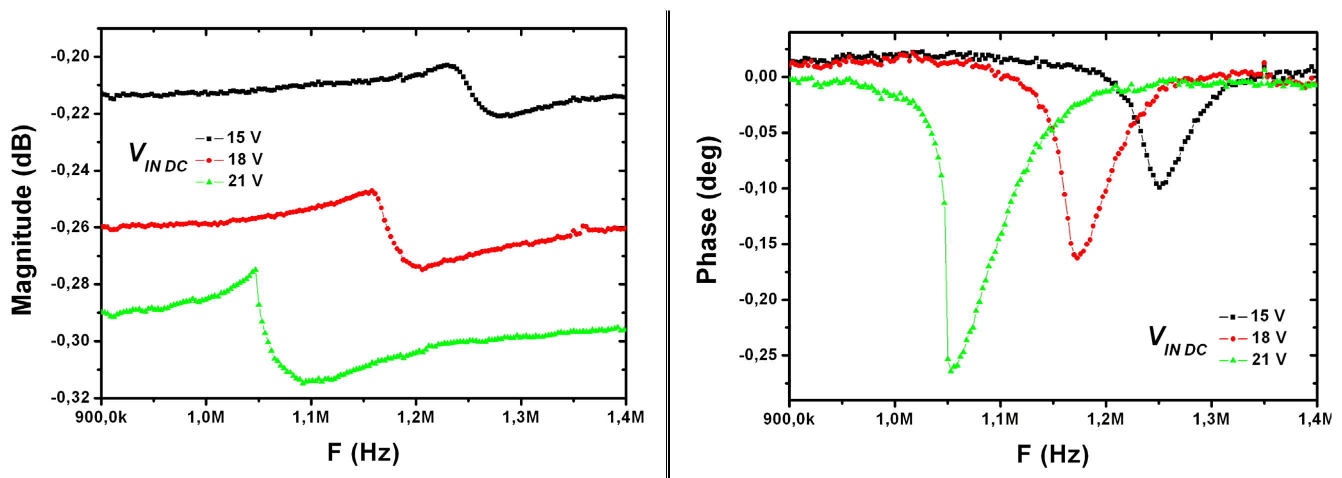

Figure 14. Calibrated resonance spectra in air of QB B for several $V_{IN\,DC}$ voltages, and $V_{IN\,AC}$=0.9 V pp

Their thinness (about 450 nm) makes that from about $V_{IN\ DC}$ =20 V on, they exhibit a nonlinear behavior (the critical oscillation amplitude mostly depends upon the thickness in the direction of vibration) what intrinsically limits the possibility to polarize QB at high voltages.

III.2.b.ii) Measurements in vacuum with set-up 2

The chip containing QB A has been wire bonded and has been measured in the vacuum chamber of set-up 2. Figure 15 depicts spectra measured at P= 1.1 10^{-2} mBar without calibrating the background signal. Lower driving voltages than in air are enough for polarizing the devices: 4 V DC added to a 0.032 V AC. All spectra exhibit a strong nonlinear behavior yielding almost vertical slopes both in magnitude and in phase. However phase changes are still smaller than 1 °, what makes almost impossible a future implementation in close loop. The Q factors are in the order of 5000-6500.

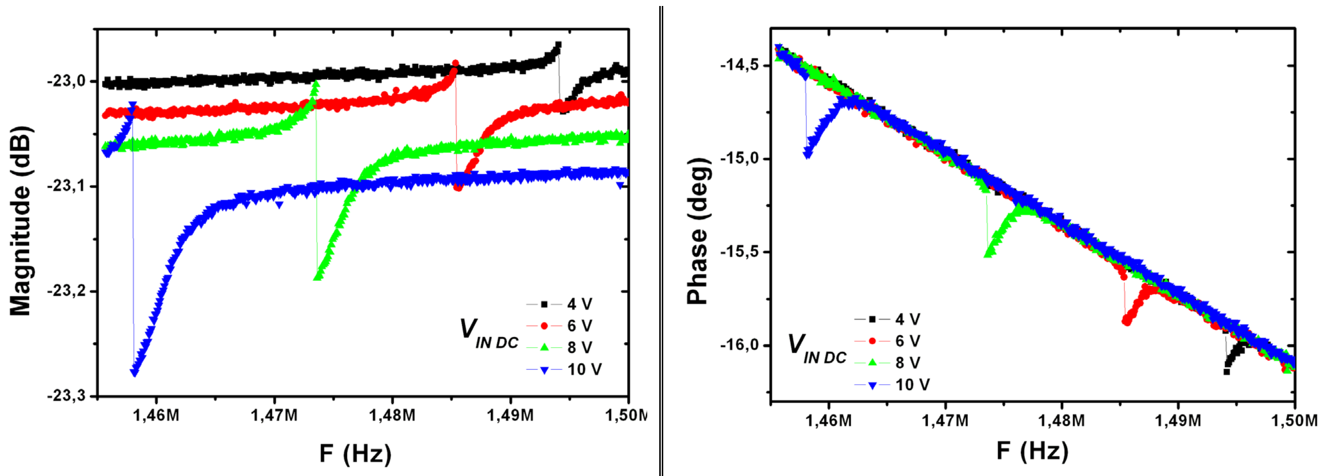

Figure 15. Non-calibrated resonance spectra in vacuum (P= 0.011 mBar) of QB A for several $V_{IN\ DC}$ voltages and $V_{IN\ AC}$ =32 mV pp.

III.2.b.iii) Electrical Results Summary

The electrical results of QB A and B are summarized in Table V - 11 and Table V - 12.

Table V - 11 reports data of calibrated measurements. $\Re$(dB) means the background signal level and ΔG(dB) the relative amplitude of the resonance peak of the calibrated signal. I_{RES_EXP} and I_{RES_TH} are obtained following the method exposed for Table V - 3.

QB	R_{LOAD} R_{POL}	V_{PI} (V)	$V_{IN\ DC}$ (V)	$V_{IN\ AC}$ (Vpp)	Q	$\Re$(dB) BS	ΔG(dB)	I_{RES_EXP} (nA)	I_{RES_TH} (nA)
A	932Ω 187kΩ	60	20	0.7	32	-24	0.0115	0.63	1.76
B	923Ω 183kΩ	52	15	0.9	32	-24	0.0108	0.77	1.88
			18				0.0129	0.91	2.71

Table V - 11. Results of electrical measurements obtained with background signal calibration.

Table V - 12 reports data without background signal calibration. G(dB)BS means the background signal level and G(dB)Res the amplitude of the resonance peak. I_{RES_EXP} and I_{RES_TH} are obtained following the method exposed for Table V - 3.

QB	R_{LOAD} R_{POL}	V_{PI} (V)	$V_{IN\ AC}$ (mV pp)	$V_{IN\ DC}$ (V)	Q	P (mBar)	G(dB) BS	G(dB) Res	I_{RES_EXP} (nA)	I_{RES_TH} (nA)
A	932Ω 187kΩ	60	32	6	6440	0.011	-23.025	-22.98	0.13	1.41
				8	5500		-23.055	-23	0.15	2.1
				10	4300		-23.082	-23.02	0.17	2.6
				4	6700	0.011	-22.995	-22.969	0.073	0.65
					7000	0.12	-22.995	-22.972	0.064	0.68
					2600	1	-22.995	-22.974	0.059	0.25
					561	10	-22.989	-22.981	0.022	0.055

Table V - 12. Electrical measurements results obtained without background signal calibration.

The pull-in voltage is interestingly high but as explained before it has not been possible to polarize higher than 25-30 V.

Concerning the accuracy of the RLC model for QB, the experimental value of I_{RES_EXP} is systematically smaller than I_{RES_TH} by a factor comprised between three and ten. This is probably due the conjugation of two factors. First, the Q factor is difficult to extract because of the low signal levels, and the method used here probably slightly overestimates the Q, what contributes to calculate too high values of I_{RES_EXP}. Second, the RLC model depends on a linear restoring force and the problem here is to accurately estimate k_{QB}, the QB spring constant. The anchor underetching makes very difficult the determination of simple expression for k_{QB}. Moreover, as it will be explained later, these structures are stressed (what is consistent with the polycrystalline nature of the material) what puts in question the use of a linear RLC model based on an elastic constant k_{QB}. Even so, the RLC model remains a good qualitative model to predict within one order of magnitude the signal levels generated by a polysilicon QB.

III.2.c. Analysis of results

Different features of the experimental behavior of quad-beams are analyzed in this section.

III.2.c.i) Estimation of the fringing field parasitic capacitance C_{PA}

In order to estimate C_{PA}, a comparison is made between experimental curves and simulated resonance spectra obtained with real parameters. The extracted value, obtained by fitting the level of background signal, is compared to the value of the capacitance related to the four anchors area.

For QB A and B, the capacitance related to the anchors is calculated around 80 fF. This value is in good concordance with the results provided by the simulations that fit the experimental curves of QB A and B. This confirms the assumption that C_{PA} is generated by the anchor capacitor.

III.2.c.ii) Q factor evolution as a function of the pressure

In Figure 16 and Figure 17, the Q factor is extracted from resonance spectra measured at different levels of pressure and maintaining all the other parameters constant.

From Figure 17, it seems that the most pronounced evolution occurs above 0.1 mBar like for cantilevers: this pressure level seems to represent a threshold below which no major improvement is achieved.

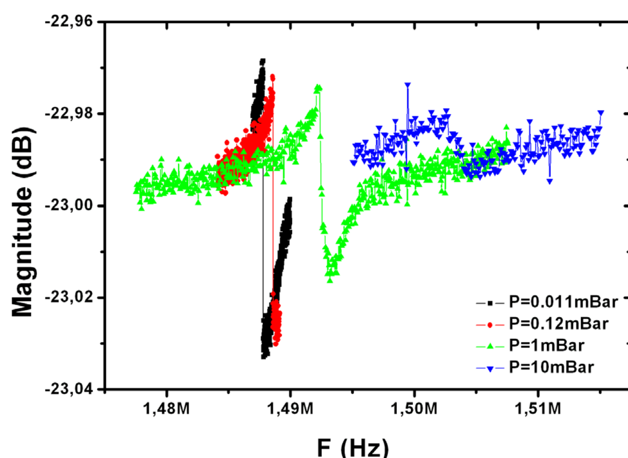

Figure 16. Non-calibrated resonance spectra of QBA recorded at different levels of vacuum for $V_{IN\ DC}$=4 V and $V_{IN\ AC}$=32 mV pp.

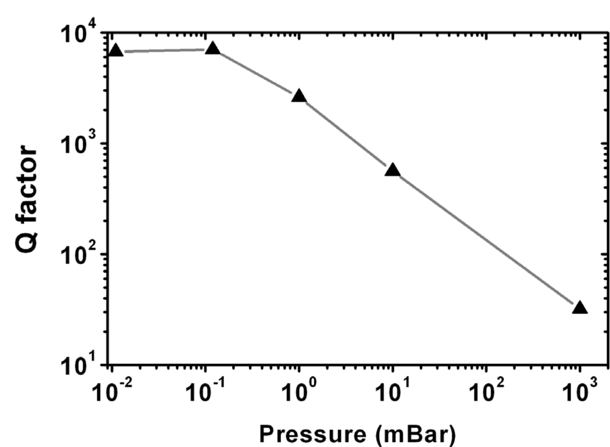

Figure 17. Corresponding dependence of the Q factor upon the level of vacuum

One can notice from Figure 11 and Figure 17 that cantilevers and quad-beams exhibit similar dependences of their Q factor upon the level of vacuum (qualitatively and quantitatively). This means that both resonators are affected in a similar way by viscous damping at ambient pressure and that they have similar mechanisms of intrinsic dissipation (clamping losses, etc… see chapter 1).

III.2.c.iii) Driving voltage effects

In the case of cantilevers, it has been systematically observed that the driving voltage ($V_{IN\ AC}$ + $V_{IN\ DC}$) has a spring-softening effect on the resonance frequency and that it tunes it down. In the case of QB, this statement is not always true and in our samples every sample has exhibited its own behavior depending upon one critical parameter: its upwards or downwards curvature.

Indeed, the key parameter that seems to determine the effect of the driving voltage is the initial curvature caused by the stress of the structural polysilicon layer (deposited on top of a SiO_2 layer). Just after their release, several QB located on the same chip have been inspected with a CONFOCAL microscope.

In almost all the QB, the central plate is curved upwards of between 150 and 300 nm with respect to the anchor. However, one (let us call it QB C) was curved downwards by 300 nm (on other chips the same was observed in the same proportion: less than 10 % in number of devices). It seems that there is a correlation between the initial curvature and the effect of the driving voltage.

QB with initial upward curvature tend to feature spring-softening effect like in Figure 18 while QB with initial downward curvature tend to feature the contrary, in other words what could be called 'spring-stiffening' effect like in Figure 19 and Figure 20 (curves of QB C).

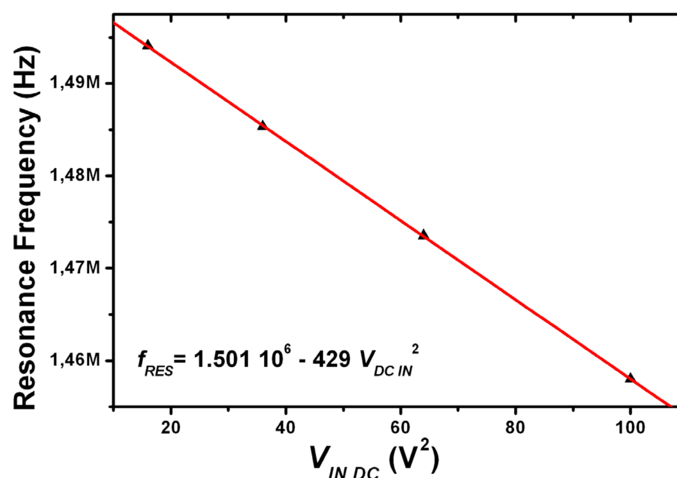

Figure 18. Based on data of Figure 15, resonance frequency dependence upon $V_{IN\ DC}$

Based on the study done in chapter 2, qualitative explanations can be proposed. Concerning QB initially curved upwards, the electrostatic force created by the driving voltage attracts them downwards, therefore the mechanical strain tends to decrease as they go towards their relaxed flat position. In these conditions, the electrostatic force dominates and spring softening effect occurs.

Concerning QB initially curved downwards, the electrostatic force created by the driving voltage also attracts them downwards, but in this case the strain tends to increase as they are more

pulled away from the equilibrium position. This creates a situation similar to the case of a stretched guitar string: the QB is mechanically stiffened. This behavior dominates over electrostatic attraction and 'spring stiffening' effect occurs (also named 'hard-spring' effect). This probably remains true while the gap is not to narrow otherwise electrostatic force would probably dominate again.

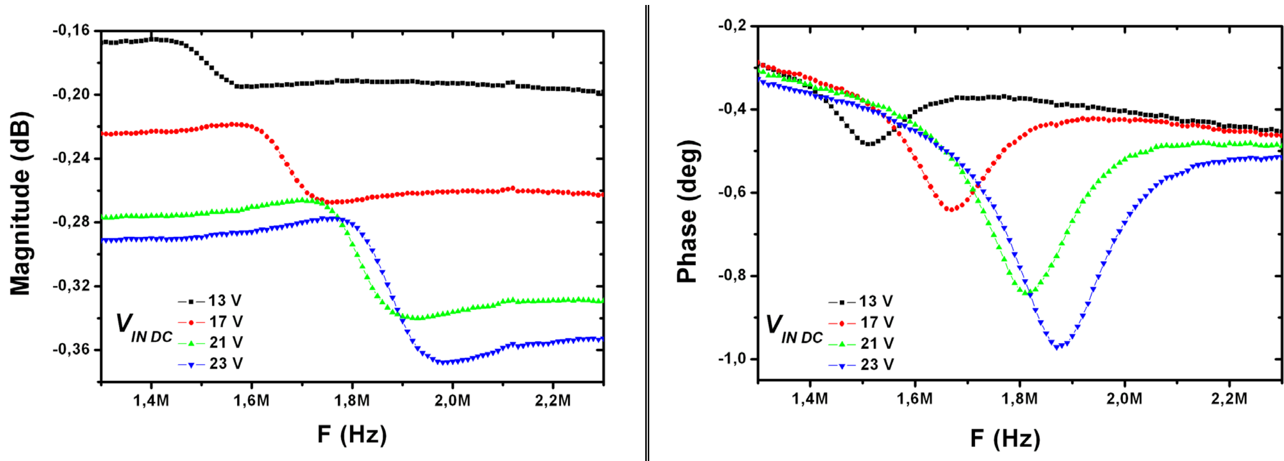

Figure 19. QB C frequency response as a function of DC driving voltage: magnitude (left) and phase (right)

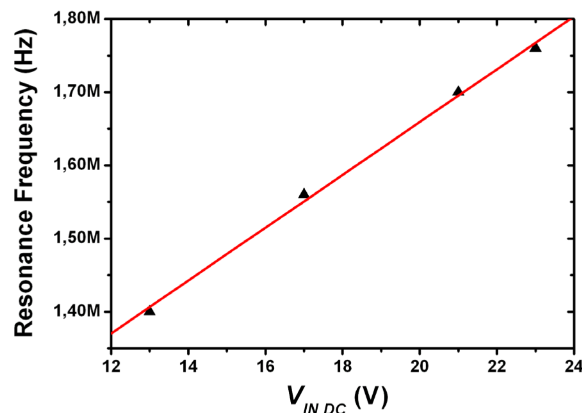

Figure 20. Resonance frequency dependence of QB upon the driving voltage

Conclusion of chapter 5

Following a capacitive detection scheme, the mechanical resonance of fully integrated nanomechanical resonators, cantilevers and quad-beams, has been successfully sensed by the CMOS circuitry. Cantilevers and quad-beams have exhibited quality factors in vacuum up to 9500 and 7000 respectively. The resonance frequency could be tuned by varying the driving voltage and interesting hysteretic nonlinear behaviors have been observed either in air or in vacuum.

These results also demonstrate that the correct operations of both the CMOS circuit and the general system are not degraded by post-processing technologies based on nSL or eBL.

The RLC electromechanical model is found to be more qualitative than quantitative but the high number of uncertainties regarding the resonators parameters (Young modulus, exact dimensions, underetching, etc...) impedes to conclude more definitively on the model accuracy. At least, this model is precise enough to predict resonance signal levels within one order of magnitude what is actually sufficient to define the specifications of a CMOS readout circuit.

As future prospects, several improvements regarding the design of the resonator could allow obtaining better electrical responses with the same circuit topology. In the case of quad-beams, the integration area should be placed farther from the circuit area so that it can be polarized at much higher voltages without perturbing the operation of closely located MOS transistors. In order to reduce ‘vertical’ (out-of-plane) stray capacitances, the pads area should be minimized. This could be achieved by incorporating holes in the central plate so that the etching time would be reduced and smaller anchors would be enough to support the structure. Concerning the cantilevers, optimizing the design of the readout and driving electrodes could lead to an important reduction of the fringing field parasitic capacitance.

After demonstrating the successful fabrication and the correct operation of CMOS integrated nano/micromechanical resonators, these devices have been implemented as ultra-sensitive mass sensors: this is the topic of next chapter (6).

Bibliographical references

1. Badzey, R.L. and P. Mohanty
Coherent signal amplification in bistable nanomechanical oscillators by stochastic resonance
Nature, 2005. **437**(7061): p. 995-998.

2. Buks, E. and B. Yurke
Mass detection with a nonlinear nanomechanical resonator
Physical Review E, 2006. **74**(4).

3. Mohanty, P., D.A. Harrington, K.L. Ekinci, Y.T. Yang, M.J. Murphy, and M.L. Roukes
Intrinsic dissipation in high-frequency micromechanical resonators
Physical Review B, 2002. **66**(8).

4. Xu, Y., J.T. Lin, B.W. Alphenaar, and R.S. Keynton
Viscous damping of microresonators for gas composition analysis
Applied Physics Letters, 2006. **88**(14).

5. Sharpe, W.N.
Measurement of Young's modulus, Poisson's ratio, and tensile strength of polysilicon
in the proceedings of the *IEEE MEMS*. 1997.

6. Albrecht, T.R., P. Grutter, D. Horne, and D. Rugar
Frequency-Modulation Detection Using High-Q Cantilevers for Enhanced Force Microscope Sensitivity
Journal of Applied Physics, 1991. **69**(2): p. 668-673.

CHAPTER 6

FUNCTIONAL CHARACTERIZATION

IMPLEMENTATION OF N-MEMS/CMOS AS MASS SENSORS

I. Punctual mass sensing. 181
I.1. Monitoring the evaporation of femtoliter droplets (exp. I) 181
I.1.a. Experimental set-up 182
I.1.b. Results and analysis 186
I.2. Double cantilever resonators (exp. II) 189
I.2.a. Features of double cantilever devices 189
I.2.b. Results of mass sensing 195
II. Distributed mass sensing experiments 200
II.1. Monitoring the deposition of ultra-thin gold layers (exp. III) 202
II.1.a. Experimental set-up 202
II.1.b. Nanomechanical sensor 206
II.1.c. Results and analysis 207
II.2. Application of NEMS/CMOS mass sensors as positioning sensors (exp. IV) 216
II.2.a. Quasi-dynamic approach 216
II.2.b. System description 216
II.2.b.i) Alignment procedure 218
II.2.b.ii) Mass sensor requirements 220
Conclusion of chapter 6 223
Bibliographical references 224

Chapter 1 established a state-of-the-art of existing nano/micromechanical resonators implemented as highly sensitive mass sensors. Compared to quartz-crystal microbalances (QCM), they offer advantages in terms of sensitivity and system integration. In addition, if they are small enough, they can provide mass sensing with spatial resolution.

These two features, unprecedented sensitivity and spatial resolution, offer new opportunities both for nanoscience and engineering purposes. Concerning the scientific aspect,

such sensors can help in studying previously unexplored chemical, physical or biological new mechanisms. Concerning engineering and industrial techniques, they could replace QCM in a near future for the monitoring of the deposition of thin layers in semiconductor processing systems, as well as serve as positioning sensors for nanostencil lithography systems of as it will subsequently explained.

Chapters 3, 4 and 5 have given a detailed description of the modeling, design, fabrication and characterization of Si nano and micromechanical resonators monolithically integrated with CMOS circuitry for on-chip resonance signal detection and amplification. These monolithic integrated microsystems that could contain very large scale integration of arrays of resonators can potentially be fabricated in batch using standard silicon technology processes. They represent compact and portable systems getting closer to the category of system-on-chip (SoC).

Taking advantage of the large number of fabricated N-MEMS/CMOS chips, four different experiments have been designed and carried out. Experiments I and II are oriented towards punctual mass sensing and experiments III and IV towards distributed mass sensing.

Experiment I is related to the development of nanofluidics and nanodispensing. The emergence of these two techniques is actually linked to a better understanding of wetting mechanisms at these scales. Within this field, the work presented here represents a breakthrough: the capability of NEMS/CMOS mass sensors is used to monitor the evaporation of femtoliter droplets, i.e. volumes that are nine orders of magnitude smaller than published data.

In experiment II, it has been tested a new functionality in the operation of nanomechanical mass sensors. A new device based on a double cantilever is proposed, allowing differential mass measurements in air with a self-reference, thus directly providing the measurement uncertainty. In parallel, other interesting features of this device are introduced. Among them, the reasons why such a device could allow measuring the mass change in function of amplitude changes and not of frequency shifts, as usually done, will be exposed.

Experiments III and IV are linked together. Actually, experiment IV consists of implementing a NEMS/CMOS mass sensor as position sensitive device, concretely as an alignment sensor. CNM and EPFL are currently developing a demonstrator of quasi-dynamic nanostencil lithography system (QDS). This system is an automated step-and-repeat nanopatterning apparatus that perform successive depositions of various materials with various patterns through a movable full-wafer stencil shadow mask. In-between each deposition step, the vacuum is not broken so that high-purity deposits are obtainable. In this context, the mass sensor will help in aligning in-situ the full-wafer nanostencil with respect to the substrate to be patterned. The first sketch of this system is presented. As a first step towards the realization of this objective, experiment III has been carried out in order to demonstrate the functionality of NEMS/CMOS mass sensors and to characterize their performance as ultra-sensitive devices for the monitoring of the deposition of ultra-thin layers.

All four experiments will be successively described and their main results will be exposed. The variety of applications presented hereafter is a real proof of the versatility of NEMS-based mass sensors.

I. Punctual mass sensing.

In this section, two experiments of punctual mass sensing are described detailing the initial motivation and their potential interest as well as their practical implementation. Then, the main significant obtained results are discussed.

I.1. Monitoring the evaporation of femtoliter droplets (exp. I)

This experiment has been carried out in collaboration with Thierry Ondarçuhu and Erik Dujardin from CEMES-CNRS, Toulouse (France), whose activity is centered on the study of wetting phenomena, nanodispensing and focused ion beam (FIB)-based nano/micromachining techniques.

Manipulation and deposition of nano/micrometer scale liquid sessile (i.e. attached) droplets on surfaces is a relatively recent topic facing a major development for about ten years. Diverse techniques like microcontact printing [1], microfluidics [2, 3], inkjet printing [4], or microlever plotting [5] routinely perform micrometer scale surface patterning, then dip-pen (DPN) lithography [6] pushed the resolution limit to the deep submicron scale. These methods constitute new tools to perform very local surface patterning or functionalization: they have a great potential for instance for biological sampling, micro/nanofluidics refilling and could eventually serve as a way to correct layout or pattern defects in IC.

In this context, CEMES has developed a novel nanoscale dispensing system (NADIS [7, 8]) that combines the high resolution potentials of DPN with the flexibility of manipulating liquids. It is based on the transfer of liquid by direct contact with the substrate of a hollow commercial AFM tip whose apex has been milled by FIB to make a small aperture. When the cantilever is loaded on its top side with a liquid, a large number of droplets with volumes in the femtoliter to subattoliter range can be deposited on a substrate with high spatial density. The parameters influencing the size of the spots are discussed in [7]: basically the spot size is determined (i) by the hole diameter but also (ii) by the wetting properties of the solvent on the tip and on the substrate surface (hydro -phobic/philic character) and (iii) by the contact time.

The need of methods to manipulate very small liquid quantities has recently emerged, leading to the development of nanofluidics or nanodispensing techniques. The point is that at these scales, evaporation processes become important. However, previous comprehensive studies have only given precise descriptions of the evaporation mechanisms for microliter droplets [9] (diameter in the millimetre range). The question of the validity of the macroscopic model for droplets with diameters in the micro and nano-scale (sub-femtoliter range) still has to be addressed.

In this context, we present a time-resolved study of the evaporation in air of sessile droplets with diameters in the µm range, what corresponds to volumes of femtoliters and smaller, i.e. nine orders of magnitude smaller than presently published data. The droplets have been deposited by NADIS and nanomechanical resonators have been used to determine with high precision the change in mass of liquid droplets with time.

I.1.a. Experimental set-up

The experiment has been based on employing CMOS integrated QB resonators as mass sensors for the monitoring of the droplet mass decrease along the evaporation process.

SENSOR DESIGN AND FABRICATION

The nanomechanical device used as mass sensor is a quad-beam resonator (QB). These QB (Figure 1) have been defined by electron-beam lithography on pre-fabricated CMOS substrates according to the process described in chapter 4 and with the CCII circuitry presented in chapters 3 and 5. Consequently, these resonators must have a resonance frequency limited to 2-3 MHz (because of the CMOS technology). Thus, devices have been adequately designed in order to have such resonance frequencies and a punctual mass sensitivity in the order of 100 attogram (10^{-16} g). Typically, they have the following dimensions (like QB *A* of table V.10): plate width and beam length around 10 µm, thickness and beam width in the submicron scale.

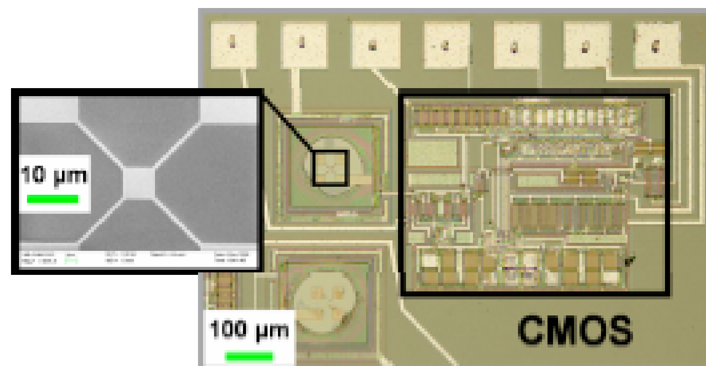

Figure 1. Optical image of a CMOS integrated QB. The device has the following dimensions: central plate 6*6 µm², beams width and length: 600 nm and 13.5 µm, thickness: 450 nm.

The QB is particularly adapted to mass measurements in air of any solid (particles, molecular aggregate) or liquid (sessile droplets of any nature) compounds. In addition to its high mass sensitivity, the QBR operated in its out-of-plane flexion fundamental mode provides a large active area for convenient droplet depositions: the alignment of the dispensing probe with the QB sensor is considerably easier than for example with narrow cantilevers.

In the QB design, the central plate is located at the extremity of the four beams what ensures that it undergoes the maximum deflection (i.e. the point where the mass sensitivity is the highest [10]). Also, when depositing a punctual mass only on the central plate and operating it in the out-of-plane fundamental mode, the QB should remain relatively insensitive to the adsorbate stiffness [11] and to the induced surface stress [12]: these assumptions ensure that the mass loading effect is mechanically dominant over stiffness (i.e. spring constant) variations. In the same perspective, the position of the adsorbate on the plate should not have any effect [10, 13] as it is assumed that the plate remains flat and uniformly undergoes the same (maximized) deflection.

The electrical detection (capacitive) scheme is non-invasive with respect to evaporation processes as it does not interfere with the specie to measure. On the contrary, laser-based optical detection techniques would have likely perturbed the measurement: the heat dissipated by the

laser spot onto the plate surface would have artificially accelerated the evaporation and diminish its duration.

In comparison, the electrical detection is not optimal neither since relatively low resonance signal levels are obtained because of the high feed-through capacitances inherent to QB. But at least the detection technique does not interfere with the evaporation process.

SENSOR CALIBRATION

Prior to the evaporation experiments, QB were calibrated (Figure 2) by successively loading, using a micro-manipulator, 1, 2, 3, and 4 silica beads whose mass is well-known (diameter of 1.57 µm and density of 2.18 $g.cm^{-3}$). The resulting resonance frequency shifts are measured and reported in Figure 2. The calibration curve (CC) constitutes a very useful and accurate reference for subsequent droplets mass measurements.

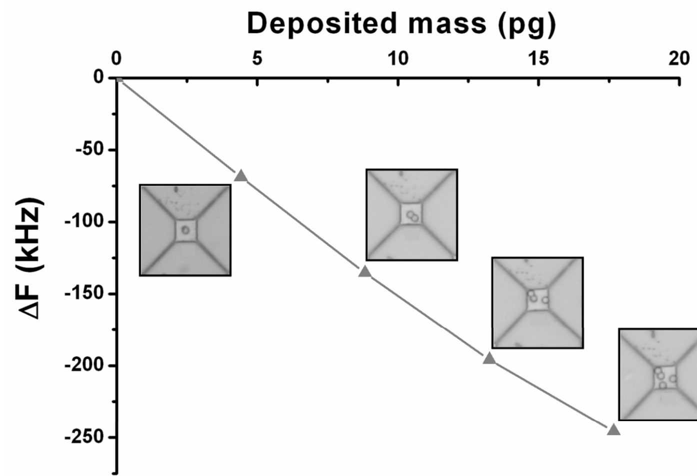

Figure 2. Calibration curve of the QB mass sensor obtained by successive loading of 1, 2, 3 and 4 silica beads, 4.4 pg each, using a micro-manipulator. The resulting resonance frequency shift is plotted as a function of the deposited mass.

For a deposited mass smaller than 5 pg, the CC follows a linear trend whose slope is the punctual mass sensitivity S. For small variations around the resonance frequency f, S is given by eq. (VI.1) (see eq.II-46):

$$S \cong 2\frac{m_{EFF_P}}{f} \qquad \text{(VI.1)}$$

where m_{EFF_P} is the efficient mass of the resonator for a punctual mass loading. From Figure 2, and for small variations around the unloaded resonance frequency, S is estimated around 6.4 10^{-17} g.Hz-1.

This value is not the intrinsic mass sensitivity of the resonator but the one valid only for a given $V_{IN\ DC}$ voltage. Indeed, the QB sensors used here are subject to spring-softening effect and according to eq.(VI.1) spring-softening tends to artificially decrease f what slightly degrades S. Therefore, it is important to emphasize that this calibration curve is valid only at the $V_{IN\ DC}$ voltage whereby it was obtained (22 V in this case) and that all mass experiments done with the QB of Figure 2 must be performed precisely at this voltage.

However, for a **larger** deposited mass, the CC does not follow any more a linear trend as shows Figure 2, not because of a loss of linearity (see chapter 2) but simply because eq.(VI.1) cannot be considered constant anymore as *f* decreases according as some mass is deposited. For large variations, the quotient of eq.(VI.1) tends to increase as *f* decreases: this is why in Figure 2 the slope tends to get flatter. In that case, the resonance frequency variation can be generalized by eq.(II-53):

$$f_{RES} = f_U \sqrt{\frac{m_{EFF_P}}{m_{EFF_P} + m_{DEPOSITED_PUNCTUAL}}} \quad \text{(VI.2)}$$

where f_U is the initial unloaded resonance frequency (actually determined by the level of V_{INDC}), m_{EFF_P} is the efficient mass of the resonator for a punctual mass loading, and $m_{DEPOSITED_PUNCTUAL}$ is the quantity of deposited mass.

m_{EFF_P} is calculated based on eq.(II-36):

$$m_{EFF_P} = m_{PLATE} + \frac{33}{140} m_{BEAM} \quad \text{(VI.3)}$$

The frequency shift is plotted in Figure 3 as a function of the deposited mass, comparing the theoretical expression provided by eq.(VI.2) and the experimental data of Figure 2, and indicating the line with constant sensitivity given by eq.(VI.1). The theoretical curve is fitted adjusting the efficient mass of the resonator m_{EFF_P} to 38 pg, very close to the nominal value of 42 pg calculated from the dimensions measured by SEM. Both theoretical and experimental curves are in good agreement:

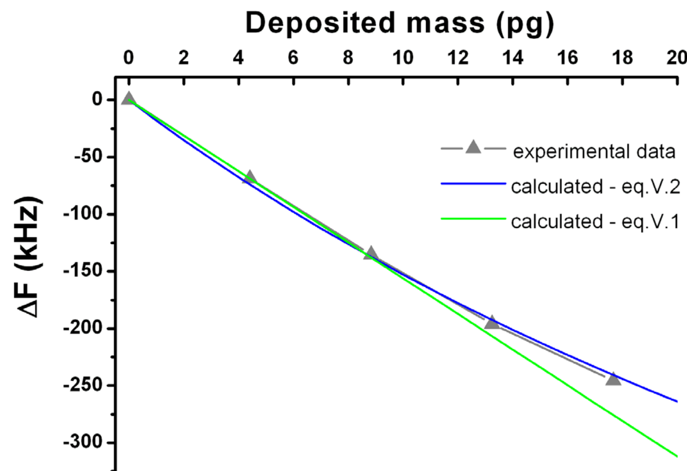

Figure 3. Comparison between the experimental data of Figure 2 and the theoretical curves given by eq.(VI.2) and (VI.1)

With the information provided by the calibration and considering small mass accretions, the performance of the QB mass sensor is compared to the one of commercially available quartz-crystal microbalances (QCM). Given the low Q-factors of QB in air (approx. 35), a minimum detectable frequency shift Δf_{MIN} of 1000 Hz is arbitrarily fixed while for QCM a value of 0.005 Hz is proposed, corresponding to the best commercially available device operated in the optimum conditions. The resulting minimum detectable mass Δm_{MIN}, given by $\Delta m_{MIN} = \Delta f_{MIN} \times S_{PUNCTUAL}$, is reported in Table VI - 1:

Device	S_{AREAL} (g.cm^{-2}.Hz^{-1})	$S_{PUNCTUAL}$ (g.Hz^{-1})	Δf_{MIN} (Hz)	Δm_{MIN} (pg)
QCM	$1.23 \cdot 10^{-8}$	$1.84 \cdot 10^{-8}$	0.005	92
Si QB	$1.8 \cdot 10^{-10}$	$6.4 \cdot 10^{-17}$	1000	0.064

Table VI - 1. Comparison between commercial QCM and silicon QB in terms of distributed and punctual mass sensitivity, frequency resolution in air and resulting mass resolution in air.

The obtained mass resolution of Si QB is three orders of magnitude better than the commercial QCM one. Although QCM have an outstanding frequency resolution, they suffer from a poor mass sensitivity. On the contrary, Si QB have a poor frequency resolution (furthermore this value is arbitrary and could be optimized) but a very high mass sensitivity.

The silica beads used for QB calibration have a mass in the order of the mass of the droplets to measure, i.e. few pg. In this context, the QCM would not have been able to measure them as its resolution is 92 pg. This explains why already published evaporation studies [14, 15] are limited to microliter droplets: it is because they are carried out with QCM.

In this experiment, the objective is to monitor the mass decrease from its initial value m_0 until about $m_0/10$. If $m_0/10 = 0.064$ pg (i.e. the detection limit Δm_{MIN} in Table VI - 1), the corresponding minimum initial diameter of the droplet is in the order of 1.5/2 µm, also depending on the hydrophilic character of the QB surface (hydrophobic surfaces result in bigger volumes for a fixed diameter). This size fixes the aperture size of the NADIS probes.

NADIS PROBES AND DROPLETS DEPOSITION PROCEDURE

Nanodispensing of droplets is performed using the technique described in [7], based on a modified AFM set-up. NADIS tips are fabricated by modification of commercially available AFM Si_3N_4 cantilevers (Olympus OMCL-RC800RP) by FIB milling. They allow dispensing droplets through a small hole milled at the tip apex (these tips are hollow pyramidal square-shaped). Whereas droplets as small as 75 nm in diameter can be obtained [7], tips with an aperture of 300 nm in diameter (see Figure 4) and hydrophilic outer walls were prepared in order to deposit micron-sized droplets, according to the QB resolution.

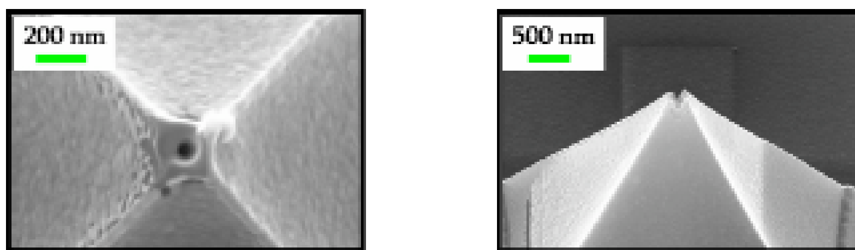

Figure 4. SEM images of modified AFM cantilever tip apex milled by FIB to form an aperture for liquid nanodispensing. (left) common NADIS probe with an aperture of 35 nm in diameter for nanoscale droplets; (right) custom NADIS probe made for this experiment with a bigger aperture of 100 nm in diameter

All the experiments were performed with glycerol-based solutions. The liquid is loaded on the modified cantilever tip with a micropipette connected to a microinjector (NARISHIGE) and controlled by a micromanipulator (THE MICROMANIPULATOR Inc.). Due to its very low volatility (boiling point, 290 °C, vapor pressure, 25 °C), the evaporation of the glycerol big accretion on top of the cantilever can take several hours.

For depositing, the tip is approached a few micrometers from the surface. Alignment with the resonator is then performed using a nanopositioning table (Figure 5) incorporated in the sample holder of the AFM set-up [16]:

Figure 5. Experimental set-up

Droplets with diameters ranging from 1 to 5 μm were reproducibly deposited on the resonators (Figure 6) by engaging the tip on the QB surface: the droplet size can actually be modulated by adjusting the contact time. This method was soft enough to keep the resonator properties intact (the same resonance frequency before and after tip contact is maintained).

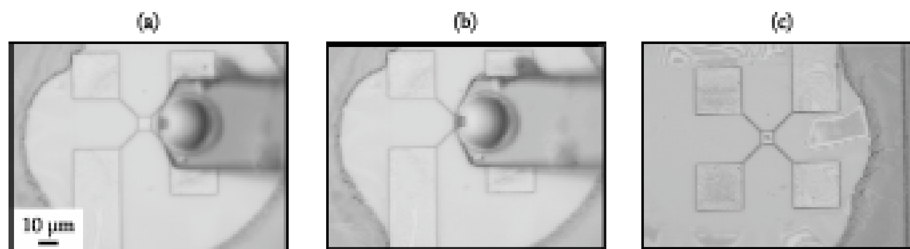

Figure 6. Top view of a nanodispensing probe (NADIS). (a) the tip, pre-loaded with a liquid, is approached; (b) it is aligned with a QB adjusting its position with the control table; (c) final image of the deposited droplet on the QB central plate.

I.1.b. Results and analysis

During evaporation, the resonance frequency of the QB (Figure 7) is monitored. Using the calibration curve, the evolving frequency shifts are converted into mass variations so that the temporal evolution of the droplets mass is determined down to around 10 fg (10 attoliters volume) resolution. The curves are rather noisy due to limitations in the experimental set-up.

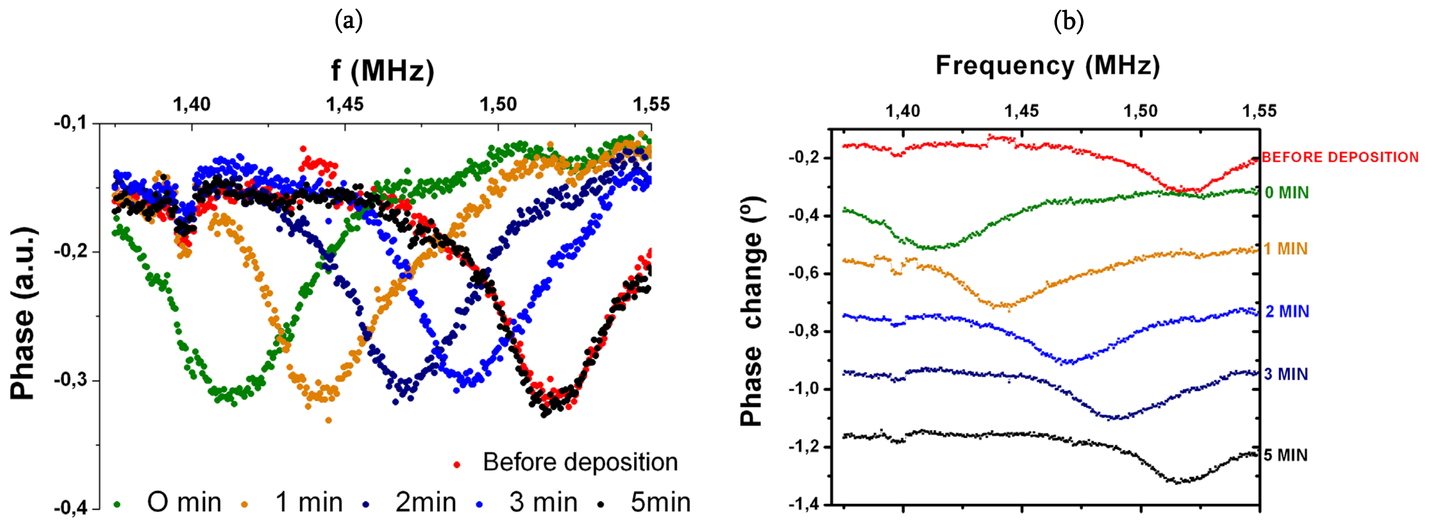

Figure 7. Evolution of the resonance frequency of a QB as a function of the evaporation time (unloaded resonance frequency ≈ 1.5 MHz) during the evaporation of a µm-sized droplet deposited by NADIS. (a) Standard curves with the same phase scale. (b) An offset is introduced between each curve in order to visualize the displacement of the phase peaks

The fact that the resonance frequency turns back to its initial value at the end of the evaporation process demonstrates that no extra particle is brought by the tip onto the surface and that the tip does not deform the QB above its elastic limit when depositing the droplet.

Time evolutions of the evaporation of glycerol droplets with initial volumes ranging from 0.2 fL to 20 fL are shown on Figure 8. The droplet mass decreases nonlinearly, with a slowing down of the evaporation rate along the process.

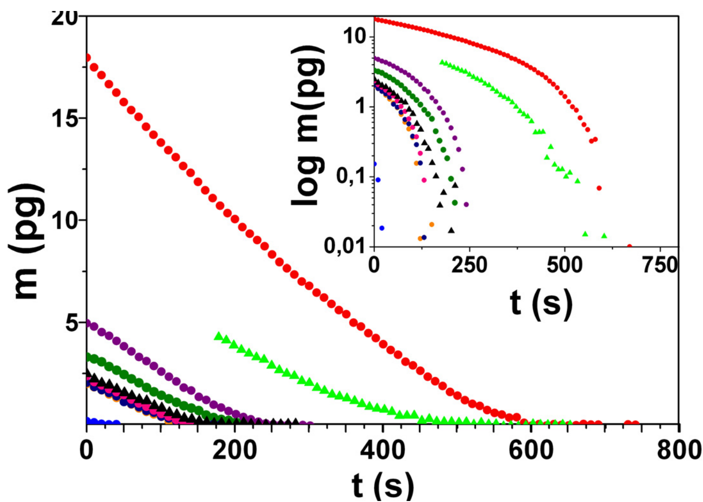

Figure 8. Temporal evolution of the mass of droplets of different initial sizes (initial volumes ranging from 0.2 fL to 20 fL). The inset plots the same data with logarithmic scale for the mass.

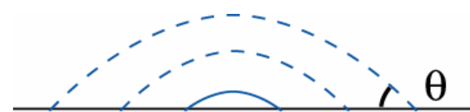

Figure 9. Constant contact angle evaporation mode on hydrophobic surfaces

It has been optically observed along the evaporation process that the droplets diameter decreases as a function of the time. This is actually characteristic of an evaporation mode taking place on hydrophobic surfaces with a constant contact angle between droplet and surface (see Figure 9). In this regime, at macroscopic scale, the droplet mass m is expected to decrease along the evaporation time with a power law 2/3 [9]:

$$m^{2/3} = m_0^{2/3} - \frac{2}{3}\alpha t \qquad \text{(VI.4)}$$

where α is a coefficient depending only on the diffusion coefficient and not on the mass, and m_0 is the initial mass.

This equation has two implications: (i) first, $m^{2/3}$ is linear with respect to the evaporation time and (ii) second, the total evaporation time t_E (at m=0) must be proportional to the initial size at power 2/3 ($m_0^{2/3}$).

To check if this macroscopic model is still valid at these scales, $m^{2/3}$ is plotted in Figure 10 (same data as in Figure 8) as a function of time: a linear decrease with the same slope is observed for every droplet. The inset also shows that the total evaporation time t_E effectively depends on the initial mass m_0 at power 2/3 (the slope of the logarithmic plot is 2/3). Both assumptions are confirmed.

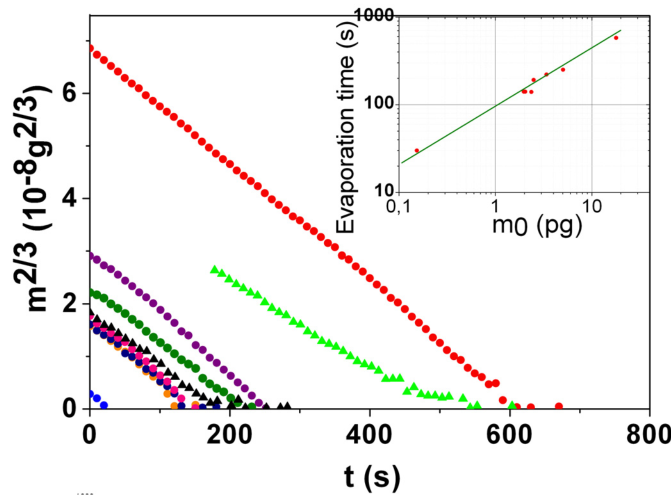

Figure 10. Temporal evolution of the droplet mass at a power 2/3 for the same data as in Figure 8. The inset is a logarithmic plot of the total evaporation time as a function of the initial mass.

Furthermore, according to eq.(VI.4), the term $m_0^{2/3} - m^{2/3}$ should be identical for every droplet since it depends only on the time and on α which is independent of the mass. This term is plotted as a function of the time for six different droplets in Figure 11:

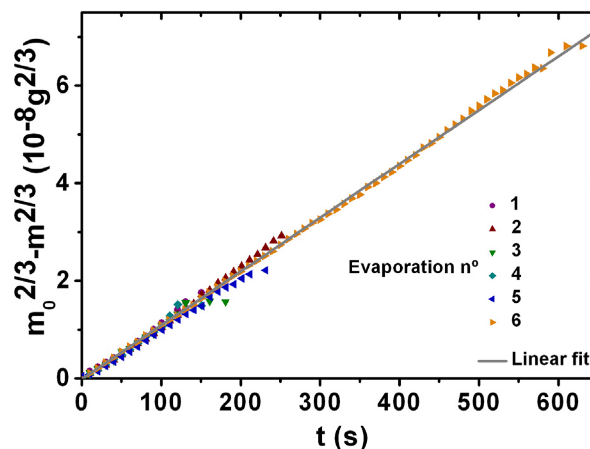

Figure 11. Plot of the term $m_0^{2/3} - m^{2/3}$ as a function of the time, for six different droplets

The curve is almost identical for six droplets which have different initial sizes. The results of Figure 10 and Figure 11 indicate that the macroscopic laws are still valid at these scales. Values of diffusion coefficients or vaporization heat extracted from these data are presently being compared with macroscopic values.

CONCLUSION

This experiment made in collaboration with CEMES provides a new knowledge of wetting mechanisms until the femtoliter range (micron scale droplet diameters) confirming the validity of macroscopic models down to these scales. Furthermore, it confirms the high potential in terms of mass sensing of CMOS integrated nano/micromechanical devices.

In order to explore the behavior of deep submicron scale droplets, and even below (100 nm scale), the resonator should be operated at higher frequencies to improve its sensitivity and selecting another design, for example cantilevers, more sensitive regarding the punctual mass sensitivity. In this experiment, cantilevers were not utilized due to their too reduced width compared to the droplet size but for depositions of droplets with diameters in the range of 100-500 nm, the cantilever narrowness would not be a limitation anymore.

Another parameter to take into account is that the evaporation time will be much shorter with nanometer scale droplets. This will oblige the mass sensor to have a much faster response time. To circumvent this issue, a closed-loop implementation of the resonator is being studied.

I.2. Double cantilever resonators (exp. II)

Chapter 1 established a state-of-the-art of existing implementations of nano/micro mechanical devices as mass sensors illustrating the recent strong interest on this topic. In this type of experiment, an important question to address is to know up to what extent the observed frequency shift is exclusively due to the mass accretion.

Towards the objective of designing a compact and portable mass sensing platform operable in ambient conditions, a reliable sensing procedure has to be defined to evaluate the measurement uncertainties which mostly arise from the formation of water thin films and from the random deposition of extra particles in suspension in air.

In order to address this issue, an innovative design that allows the direct determination of the measurement uncertainty is presented. Two closely located and almost identical (in terms of material and dimensions) nanomechanical resonators are simultaneously operated: one serves as sensor and the other as reference. In this way, rapid and reliable measurements in air are made possible.

The nanomechanical device is a polysilicon double cantilever (DBC). The DBC also features other promising properties that are detailed hereafter. Finally, the self-reference application will be emphasized describing the experimental procedure and the obtained results.

I.2.a. Features of double cantilever devices

The DBC consists of two cantilevers with the same anchor (i.e. same readout electrode) orthogonally orientated one to each other. They have been defined by electron-beam lithography on prefabricated CMOS substrates according to the process detailed in chapter 4. These DBC are

operated in their in-plane flexural fundamental mode and their oscillations are detected through the CCII circuit following the same capacitive scheme as for the single cantilevers described in chapter 3.

Both cantilevers are designated according to the nomenclature depicted in Figure 12: so-called vertical (VC) and horizontal (HC) cantilevers. Typically, these cantilevers are 14 µm long, 300/400 nm wide, 450 nm thick and have a gap comprised between 400 nm and 1 µm with respect to the driving electrode:

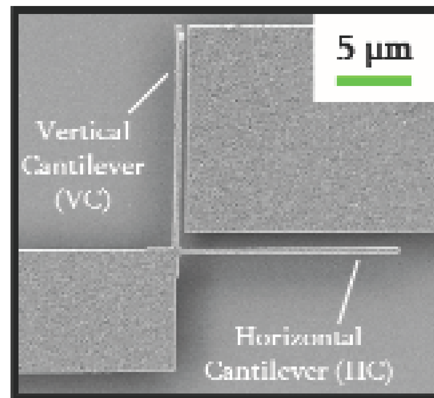

Figure 12. SEM image of a characteristic polysilicon DBC with the designation of each cantilever

In Figure 13, an overview of the integration of DBC on CMOS substrates is proposed. The inferior tilted SEM image illustrates the release.

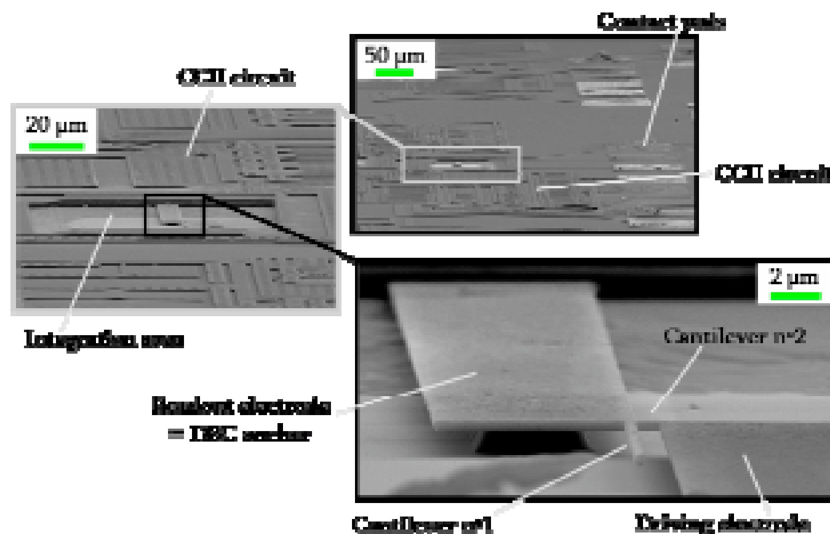

Figure 13. Tilted SEM images, with increasing magnification, of a DBC monolithically integrated into CMOS circuitry. Anchor underetching is well visible.

RESONANCE PEAKS SUPERPOSITION

The electrical frequency response of a DBC is the addition of the individual response of each cantilever. Individually, each one exhibits spring-softening effect (see chapter 3) and thereby its resonance frequency can be tuned down when increasing the driving voltage. Adjusting the voltage allows superposing both resonance peaks. In the example of Figure 14, each cantilever is independently polarized and the frequency response of each one is approximated by a Lorentzian function. The single condition is that one has a natural bigger resonance frequency than the other.

This superposition implies at least two interesting applications. First, a tunable electromechanical band-pass frequency filter could be formed through the control of the difference of resonance frequency between both. Its position and sharpness could be adjusted through the driving voltage of each one. Moreover, this concept could be extended to more than two cantilevers provided they all have the same readout electrode.

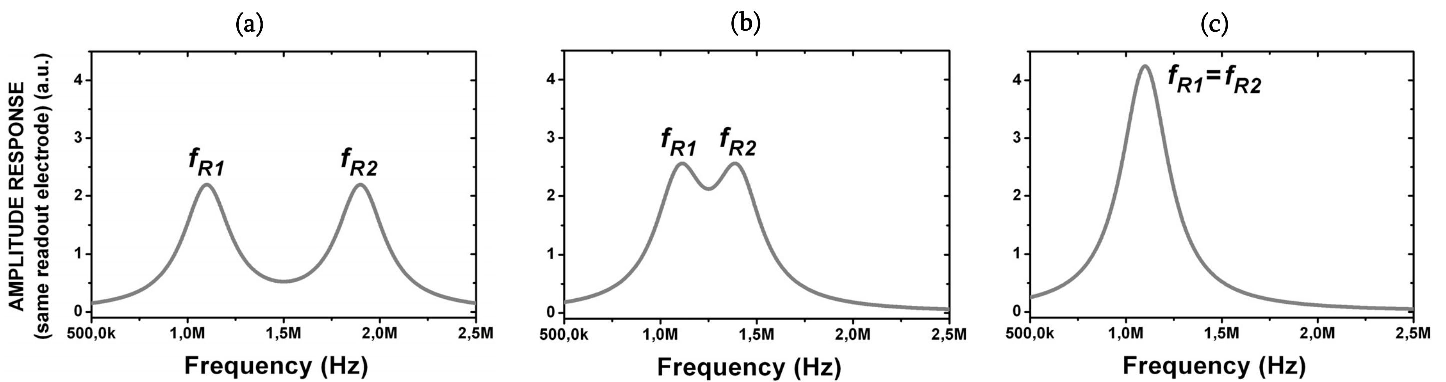

Figure 14. Conceptual representation of the global frequency response of a DBC device with common readout electrode. The cantilever with higher resonance frequency (f_{R2}) is driven from (a) to (c) with increasing driving voltage while the other (f_{R1}) is driven at a constant voltage

A second application to explore, which has not been experimentally tested yet, would consist in detecting a mass deposition through a change in amplitude of the superposed peaks instead of the classical approach relying on the measurement of resonance frequency shifts. If in the moment of starting the mass deposition, both cantilevers are driven in a way that both resonance peaks are superposed, and if only one cantilever is loaded, the combined frequency response exhibit important changes in terms of amplitude (see Figure 15) that can proportionally be much more important than changes of resonance frequency. Such an approach has already been tested but relying on mechanically coupled cantilevers [17].

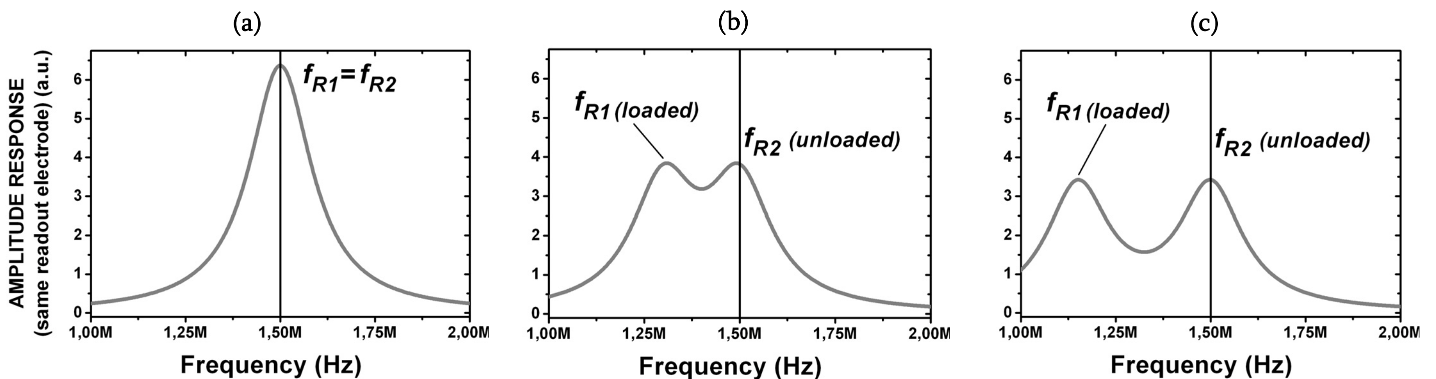

Figure 15. Conceptual representation of the global frequency response of a DBC initially operated so that both resonance peaks are superposed (a). In (b) and (c), 1 of the 2 cantilevers is progressively loaded with mass while the other remains unloaded.

In practice, superposing the two peaks is not straightforward especially if the driving electrode is common. It implies a series of requirements regarding the cantilevers design. First, one cantilever must have a higher natural resonance frequency than the other. For in-plane vibrating cantilevers, the resonance frequency f_0 and the punctual mass sensitivity S are related to the geometrical dimensions in the following way:

$$f_0 \propto \frac{b}{l^2} \qquad S \propto h\,l^3 \tag{VI.5}$$

where l, b and h are the cantilever length, width and thickness respectively

To make higher the resonance frequency of the vertical cantilever than the horizontal one, it is defined wider: $f_{0V} > f_{0H}$ with $b_V > b_H$ and $l_V = l_H$.

The resonance frequency is tuned by the DC driving voltage (assuming $V_{IN\,DAC} >> V_{IN\,AC}$) in the following way (see chapter 2):

$$f = f_0\left(1 - K\,V_{IN\,DC}^2\right) \tag{VI.6}$$

where K, the electromechanical coupling factor, is given by eq.II-81:

$$K = \frac{\varepsilon_0 l\,h}{d^3}\frac{1}{2k} = \frac{3\,\varepsilon_0 l^4}{4E\,b^3 d^3} \tag{VI.7}$$

this means in practice that with $l_V = l_H$ and $d_V = d_H$, then

$$K_V < K_H \tag{VI.8}$$

From eq.(VI.5) and (VI.7), it is clear that at same length and gap, the driving voltage dependence of the cantilever with higher resonance frequency has intrinsically a lower slope than the other. In these conditions it is impossible to superpose both resonance peaks as the curves cannot intersect (see Figure 16).

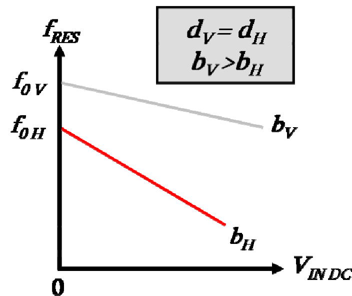

Figure 16. Dependence of the resonance frequency of the vertical and horizontal cantilevers for identical length and gap but $b_V > b_H$

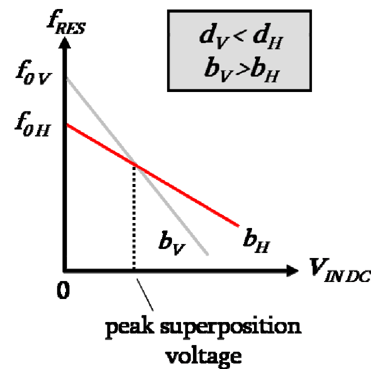

Figure 17. Dependence of the resonance frequency of the vertical and horizontal cantilevers for identical length but $b_V > b_H$ and $d_V < d_H$

The only way to intersect them is to decrease the gap of the vertical cantilever with respect to the other in order to compensate the larger width (see eq.(VI.7)).

First prototypes of double cantilevers with different gaps and widths, and identical lengths have been fabricated. However, due to deviations in the definition of dimensions by e-beam lithography and RIE, the nominal design could not be reproduced in these first tries. As a consequence, both peaks could not be superposed but the curves of Figure 18 constitute a first step towards a proof of concept:

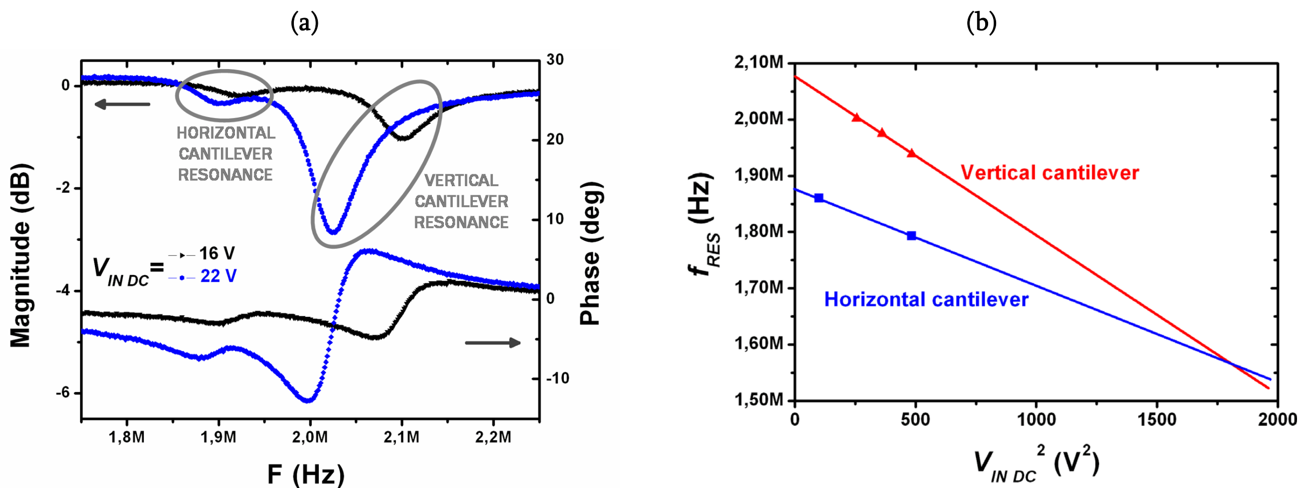

Figure 18. First experimental prototype of DBC. Both peaks are tried to be superposed adjusting the DC driving voltage. (a) resonance spectra; (b) corresponding dependence of the resonance frequency upon the driving voltage $V_{IN\ DC}$

The vertical and horizontal cantilevers (VC and HC) (see Figure 12) have a gap of 600 and 1000 nm respectively. This explains two things: first, this is why the vertical one exhibits a higher slope that would intersect the other curve at about $(42\ V)^2$ ($\equiv 1800\ V^2$) [see Figure 18(b)]. Second, this is why the resonance peak of the horizontal cantilever is so weak, the capacitive coupling is lessened owing to the wide gap. Furthermore as it can be seen in Figure 12, its readout electrode is not optimized as it is wider than the cantilever what creates a higher parasitic fringing field capacitance.

In future devices, redesigning the readout electrode and optimizing the patterning, DBC with not too different gaps could allow obtaining peak magnitudes of the same order and superposing them in a reasonable range of driving voltage (15-25 V).

MASS MEASUREMENT BASED ON AMPLITUDE CHANGE OF THE COMBINED PEAKS

Mass measurements are usually based on monitoring resonance frequency shifts. Yet, as Figure 15 illustrates it, operating the DBC so that its resonance peaks are superposed and loading mass only on one cantilever, the peak of the loaded cantilever should shift down to lower frequencies while the other remains stationary. As a consequence, the combined electrical response is modified also in terms of maximum amplitude.

Hereafter, a short demonstration is given of the interest of measuring the amplitude change as a more sensitive method than the tracking of resonance frequency shift. This is just a presentation of the concept, its experimental implementation could not be done and it must be

admitted that relying on the amplitude may not be optimum in the sense that it can experience some external fluctuations (arising from the instrumentation in general) independently of any mass loading.

Considering that the DBC is capacitively detected and that both cantilevers have a common readout electrode, let us approximate the electrical amplitude response as the sum of two frequency dependent Lorentzian functions of same magnitude, corresponding to the contribution of each cantilever centered on their respective resonance frequency $f_{RES\,H}$ or $f_{RES\,V}$. Although the Lorentz function is not the most accurate representation of a RLC//C response (that has resonance and anti-resonance peaks), it can be used as an adequate mathematical support for the demonstration:

$$A = L(f_{RES\,H}) + L(f_{RES\,V}) \text{ with } L(f_{RES}, f) = \frac{1}{\pi} \frac{\left(\frac{\Gamma}{2}\right)}{(f - f_{RES})^2 + \left(\frac{\Gamma}{2}\right)^2} \quad \text{(VI.9)}$$

where Γ is considered identical for both and equal to $\Gamma = \frac{f_{RES}}{Q\sqrt{\sqrt{2}-1}}$, Q is the Q-factor and f is the frequency. The amplitude maximum of this Lorentz function is $\frac{2}{\pi\Gamma}$ and Γ is the width at half-maximum. At the superposition frequency ($f_{RES\,V} = f_{RES\,H} = f_{SP}$, accessible with the adequate driving voltage), the combined magnitude response is maximum (A_{MAX}).

Staying in the same driving conditions, let us assume that a small mass is deposited on top of the VC, and let us compare now the ratio $\frac{\delta A}{A_{MAX}}$ and $\frac{\delta f}{f_{SP}}$. δf is the resulting frequency deviation of the VC from f_{SP} the superposition resonance frequency, and δA is the change in magnitude at the frequency $f_T = \left(\frac{f_{RES\,H} + f_{RES\,V}}{2}\right)$.

Tracking the signal at f_T is interesting since at this frequency the response offers the widest possible range: from A_{MAX} at the superposition frequency ($f_{RES\,V} = f_{RES\,H} = f_{SP} = f_T$) down to 0 when both peaks are far from each other. The magnitude corresponding to this frequency is globally given by:

$$A\left(\frac{f_{RES\,H} + f_{RES\,V}}{2}\right) = \frac{4\Gamma}{\pi\left[\left(f_{RES\,H} - f_{RES\,V}\right)^2 + \Gamma^2\right]} \quad \text{(VI.10)}$$

To compare the ratio $\frac{\delta A}{A_{MAX}}$ and $\frac{\delta f}{f}$, the following calculations are undertaken:

$$\delta A \approx \frac{\partial A}{\partial f}\delta f \quad \text{(VI.11)}$$

what results in:

$$\frac{\delta A}{A_{MAX}} = U\frac{\delta f}{f_T} \quad \text{(VI.12)}$$

where:

$$\boldsymbol{U} = \frac{1}{(\boldsymbol{A}/\boldsymbol{f})}\frac{\partial \boldsymbol{A}}{\partial \boldsymbol{f}} \approx \frac{\boldsymbol{f}_{RES\,H}\left(\boldsymbol{f}_{RES\,H} - \boldsymbol{f}_{RES\,V}\right)}{\left(\boldsymbol{f}_{RES\,H} - \boldsymbol{f}_{RES\,V}\right)^2 + \Gamma^2} \qquad \text{(VI.13)}$$

Studying the function $U(f_{RES\ V})$, we determine that U becomes superior to 1 (i.e. when the method of mass measurement based on amplitude changes becomes better) provided a minimum frequency shift δf_{MIN} is caused by mass loading:

$$\delta \boldsymbol{f}_{MIN} \geq \left(\boldsymbol{f}_{RES\,H} - \sqrt{\boldsymbol{f}_{RES\,H}^2 \left(1 - \frac{4\left(1+\sqrt{2}\right)}{\boldsymbol{Q}^2} \right)} \right) \qquad \text{(VI.14)}$$

For f_{RES} in the MHz range, δf_{MIN} is around 25 kHz for Q=10, around 250 Hz for Q=100, and around 2.5 Hz for Q=1000. The higher the Q, the wider is the improvement range in which the magnitude-based mass measurement becomes better.

Different interesting features of the DBC device have been emphasized. However, up to now our practical experimentation of the DBC has been focused only, for a matter of time, on the application of self-reference mass measurements. Hereafter, this experiment is detailed in terms of implementation and results.

I.2.b. Results of mass sensing

The objective is to establish a new method for robust and rapid mass measurements in ambient conditions. In this case, the resonator-based sensor faces two issues: (i) high air damping resulting in low Q-factors and therefore less precise measurements, and (ii) parasitic mass depositions under the form of water thin film arising from the ambient humidity and extra adsorbed particles, which introduce additional fake frequency shifts. In this context, the DBC represents an interesting approach.

The idea is to use one of the two cantilevers, on which a punctual mass accretion is deposited, to determine with high precision the amount of deposited mass by measuring its resonance frequency shift. The other cantilever also exhibits a shift, whether positive or negative, but much smaller: this deviation provides a straightforward value of the measurement uncertainty.

In terms of device design, a series of specifications can be defined. First, both cantilevers should be spatially separated enough in order to ensure that only one cantilever undergoes an addition of mass during material dispensing. However they must be closely located so that it can be considered they face the same environmental perturbations (humidity, temperature changes, particles in suspension in air, etc…). The third point is the required similarity in the dimensions: in this way, they have the same punctual mass sensitivity and any resonance frequency shift exhibited by one cantilever or the other can be quantitatively compared with respect to the other. The orthogonal design of Figure 12 is proposed but different implementations are also possible.

This auto-reference principle has been experimentally tested by very locally depositing mass accretions by FIB only at the free extremity of the vertical cantilever (i.e. where the mass sensitivity is maximum [10]).

Several tests have been carried out following an experimental procedure based on three steps:

- first, the DBC is measured in ambient conditions (not in clean room atmosphere) with the measurement set-up nº1 referenced in chapter 5. Its resonance spectrum exhibits two different peaks related to each cantilever (like in Figure 18.a). Several spectra are recorded at different driving voltages, so that the spring-softening curve f_{RES}= f($V_{IN\ DC}{}^{2}$) (like the curve of Figure 18.b) is characterized for both cantilevers.
- then, the chip is placed into the vacuum chamber of a focused ion beam (ZEISS 1560XB, GEMINI column) and a certain amount of material (a Ga/Pt/C alloy with a density of 12.5 g/cm^3) is locally deposited[1] at the tip of the vertical cantilever only (see Figure 19 and Figure 20). A typical rectangular-shape deposit is 600 nm long, 300 nm wide and 120 nm thick what represents approximately 250 fg. This operation has been realized by Gemma Rius, Jordi Llobet and Xavier Borrise at CNM.

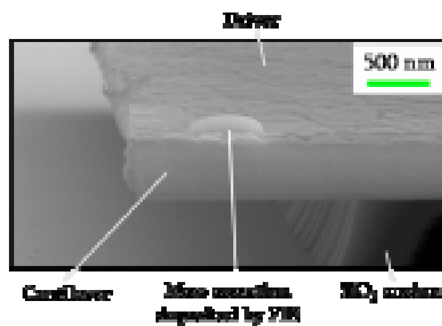

Figure 19. Tilted SEM image of the vertical cantilever tip where a mass accretion has been deposited by FIB

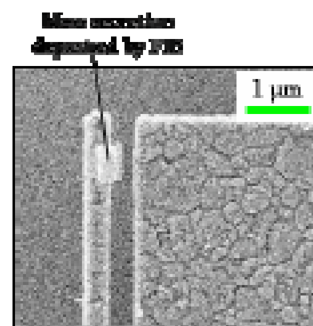

Figure 20. SEM image in top view of the vertical cantilever tip with a deposited mass accretion

- the third step consists in taking the sample off the FIB chamber and measuring it again in ambient conditions with the same electrical set-up.

Following this procedure, seven experiments have been carried out on five cantilevers. Their dimensions and their experimental (initial) natural resonance frequency are reported in Table VI - 2. The natural resonance frequency is estimated from the value extrapolated at $V_{IN\ DC}$ =0 in the spring-softening curves. The subsequent mass deposition is not supposed to modify the slope of the driving voltage dependence (given by eq.(VI.7)) as, in theory, the stiffness is not modified during the loading, especially if the mass is deposited at the end [11, 13]. The theoretical mass sensitivity of all these DBC is in the order of 1.2 10^{-18} g.Hz^{-1}.

[1] Deposition parameters: ion current 1 pA, nominal deposit area: 250*500 nm^2, exposure time 20s

DBC	Vertical cantilever				Horizontal cantilever			
	l_V (µm)	b_V (nm)	d_V (µm)	f_{EXP_V} (MHz)	l_H (µm)	b_H (nm)	d_H (nm)	f_{EXP_H} (MHz)
CD1	14.4	0.4	0.6	2.07	14.5	0.42	1	1.88
CD2	14.5	0.4	0.4	1.90	14.2	0.42	0.93	2.09
CD3	14.5	0.4	0.6	1.93	14.5	0.42	1	1.89
CD4	14.6	0.4	0.4	1.86	14.2	0.42	0.93	2.07
CD6	14.3	0.4	0.4	2.15	14.2	0.42	0.93	2.27

Table VI - 2. Initial characteristics of the five DBC used in mass sensing experiments. The thickness is around 460 nm for all of them

On each DBC, small mass accretions have been deposited only on the vertical cantilever. The sizes of the resulting deposits have been subsequently estimated by imaging them with SEM and AFM. The frequency shifts are calculated from the changes of natural resonance frequencies (that are extrapolated at $V_{IN\ DC}$ =0). All the results are reported in Table VI - 3:

Test nº (DBC nº)	f_I (MHz)	f_F (MHz)	Δf (kHz)	deposit shape	dimensions of accretion (nm³)	m_{TH} (fg)
1 (CD1)	2.07	1.89	-182	cylindrical	$\pi(200)^2/2*300$	240
2 (CD3)	1.93	1.75	-174	parallelepiped	*l,w,h* 700, 390, 120	410
3 (CD6)	2.15	2.06	-89	cylindrical	$2\pi(120)^2/3*300$	45
4 (CD2)	1.90	1.77	-137	parallelepiped	*l,w,h* 580, 310, 130	290
5 (CD3)	1.74	1.63	-110	parallelepiped	*l,w,h* 620, 390, 100	300
6 (CD4)	1.86	1.71	-149	parallelepiped	*l,w,h* 600, 320, 120	290
7 (CD6)	2.06	1.95	-108	parallelepiped	*l,w,h* 590, 270, 120	240

Table VI - 3. Results of seven depositions on five vertical cantilevers. The initial f_I and final f_F resonance frequency as well as the resulting shift are provided. The dimensions of the deposits are given

It can be noticed from Table VI - 3 that the devices CD3 and CD6 were used in two sets of experiments (separated by two weeks) and the initial frequencies of the second set (nº5 and 7) are in perfect concordance with the final frequencies of the first set (nº2 and 3).

In Figure 21, an example of resonance spectra recorded before and after FIB depositions is proposed. The reason why the peak of the HC is much weaker than for the VC is that its gap is much larger than the VC one. In future samples, simply setting an equal gap for both the VC and the HC will result in two similar peaks in terms of magnitude.

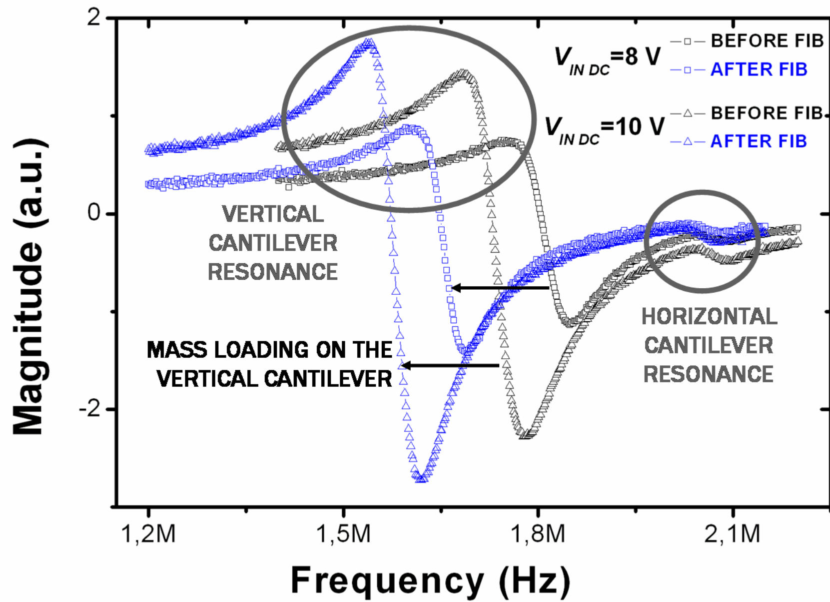

Figure 21. Resonance spectra of CD4 for two DC driving voltages before and after FIB depositions

This graph clearly illustrates the resonance frequency shift of the VC while the one of the HC remains stationary. The corresponding spring-softening curve of this device is shown in Figure 22:

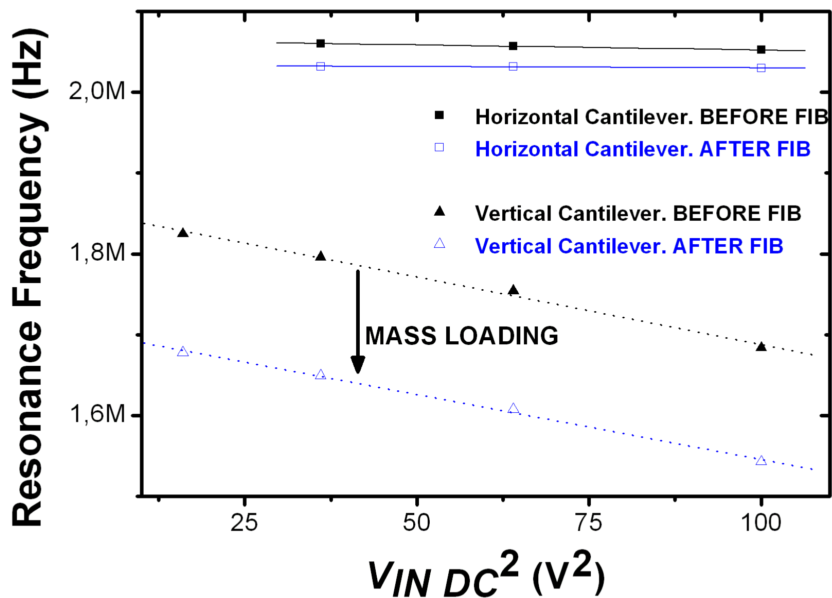

Figure 22. Spring-softening curves of CD4 (experiment nº6).
The mass is deposited only on the vertical one.

Coherently, the slope of the spring-softening curves is not affected by the deposition and the VC exhibits a clear shift downward while the HC exhibits a small shift determining the uncertainty of the measurement. The results of the seven experiments are reported in Table VI - 4. The measured frequency shifts as well as the deposits sizes are listed: the corresponding experimental sensitivity S_{EXP} is obtained making the ratio $\Delta m_{EXP} / \Delta f$ (Δm_{EXP} is the value estimated

from AFM and SEM images). The theoretical deposited mass is calculated as a function of the initial and final resonance frequency through eq.II-47:

$$\Delta m = \frac{k_{EFF_P}}{4\pi^2}\left(\frac{1}{f_F^{\,2}} - \frac{1}{f_I^{\,2}}\right)$$

where k_{EFF_P} is the effective spring constant for a punctual mass deposition at the free end.

From the frequency shifts of the HC, an uncertainty for the theoretical value is calculated.

DBC	Vertical cantilever with FIB deposition				Horizontal cant. with no FIB deposition
	Δf (kHz)	Δm_{EXP} (fg)	S_{EXP} (g/Hz)	Δm_{TH} (fg)	Δf (kHz)
1 (CD1)	-180	240	1.3 10^{-18}	405 ± 73 (18%)	+57
2 (CD3)	-174	410	2.4 10^{-18}	436 ± 61 (14%)	-48
3 (CD6)	-89	45	5 10^{-19}	166 ± 12 (7%)	-9
4 (CD2)	-137	290	2.2 10^{-18}	345 ± 8 (2%)	-6
5 (CD3)	-110	300	2.3 10^{-18}	357 ± 18 (5%)	-14
6 (CD4)	-149	290	1.9 10^{-18}	412 ± 40 (10%)	-31
7 (CD6)	-108	240	2.2 10^{-18}	209 ± 26 (12%)	-20

Table VI - 4. Results of seven depositions successively performed on five cantilevers

Masses in the range of 250-400 fg have been deposited and successfully measured with an average uncertainty of 10 % provided by the measurement of the HC shift. The experimental and theoretical values of the mass are in good concordance taking into account all the measurement uncertainties: the one arising from estimations of deposits size based on SEM/AFM images, and the other coming from environmental perturbations which are estimated from the HC shift.

In further experiments, it will be necessary to refine the spring-softening curves for a finer extraction of resonance frequency. This should be obtainable (i) optimizing the readout electrode design (to reduce the fringing field capacitance affecting the HC), (ii) assigning the same value for both gaps and (iii) recording the resonance spectra with a finer sweep of the DC driving voltage.

Present measurements have been performed in non-optimal conditions, in fact the electrical test and the FIB depositions did not even take place in the same building. Taking into account these non-optimal conditions, the DBC can provide the measurement uncertainty through the 'error shift' measured with the HC. It can be noticed that the deviation does not exceed an average of 10% and the theoretical and experimental values of the deposited mass match quite well.